

# Ordered Hydrogen-Bonded Alcohol Networks Confined in Lewis Acid Zeolites Accelerate Transfer Hydrogenation Turnover Rates

John R. Di Iorio, Blake A. Johnson, and Yuriy Román-Leshkov\*

Cite This: *J. Am. Chem. Soc.* 2020, 142, 19379–19392

Read Online

ACCESS |

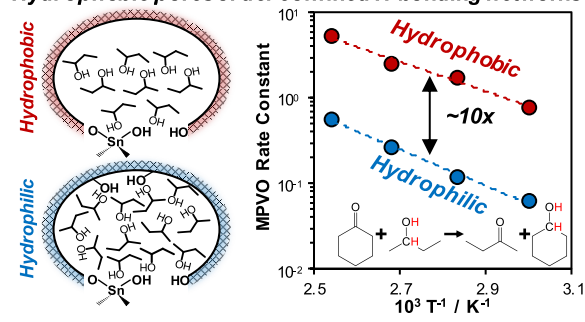
Metrics & More

Article Recommendations

Supporting Information

**ABSTRACT:** The disruption of ordered water molecules confined within hydrophobic reaction pockets alters the energetics of adsorption and catalysis, but a mechanistic understanding of how nonaqueous solvents influence catalysis in microporous voids remains unclear. Here, we use kinetic analyses coupled with IR spectroscopy to study how alkanol hydrogen-bonding networks confined within hydrophobic and hydrophilic zeolite catalysts modify reaction free energy landscapes. Hydrophobic Beta zeolites containing framework Sn atoms catalyze the transfer hydrogenation reaction of cyclohexanone in a 2-butanol solvent 10× faster than their hydrophilic analogues. This rate enhancement stems from the ability of hydrophobic Sn-Beta to inhibit the formation of extended liquid-like 2-butanol oligomers and promote dimeric H-bonded 2-butanol networks. These different intraporous 2-butanol solvent structures manifest as differences in the activation and adsorption enthalpies and entropies that comprise the free energy landscape of transfer hydrogenation catalysis. The ordered H-bonding solvent network present in hydrophobic Sn-Beta stabilizes the transfer hydrogenation transition state to a greater extent than the liquid-like 2-butanol solvent present in hydrophilic Sn-Beta, giving rise to higher turnover rates on hydrophobic Sn-Beta. Additionally, reactant adsorption within hydrophobic Sn-Beta is driven by the breakup of intraporous solvent–solvent interactions, resulting in positive enthalpies of adsorption that are partially compensated by an increase in the solvent reorganization entropy. Collectively, these results emphasize the ability of the zeolite pore to regulate the structure of confined nonaqueous H-bonding solvent networks, which offers an additional dimension to modulate adsorption and reactivity.

## Hydrophobic pores order confined H-bonding networks



## 1. INTRODUCTION

The thermodynamics of molecular adsorption from the liquid phase into a confining pocket often deviate from trends observed in the gas-phase for numerous reasons that depend on the solvent, adsorbate, and polarity of the confined adsorption site. In biological catalysts, the complexation of guest molecules from aqueous solutions with active sites results in substantial rearrangement and removal of water molecules confined within the organic scaffold, leading to compensating changes in the enthalpies and entropies of adsorption.<sup>1–3</sup> In such systems, positive entropies of adsorption are compensated by endothermic adsorption enthalpies that arise from the displacement of ordered water molecules confined within microporous hydrophobic voids (pore diameter <2 nm) surrounding the catalytic binding site.<sup>4</sup> The arrangement of various hydrophobic and hydrophilic residues within enzymatic active sites facilitates the organization of confined solvent molecules, which serves to modify reaction free energy landscapes.<sup>3,5</sup> This evolutionary ability of biological catalysts to enhance reaction rates by regulating the structure of occluded solvent molecules has stimulated interest in the design of zeolite catalysts as artificial analogues.

Siliceous zeolites are an intriguing class of microporous catalysts for liquid-phase reactions because their molecular-sized pores (<2 nm) introduce steric constraints that inhibit catalysis of molecules larger than their pore diameters via size exclusion phenomena<sup>6</sup> but also mirror biological catalysts in their ability to solvate transition states and reactive intermediates confined within their pores via dispersive interactions with the zeolite framework. Such interactions alter selectivities and rates of catalytic reactions that depend on the size and shape of the confined species and pore architecture.<sup>7–13</sup> Zeolites are constructed from nonpolar SiO<sub>2</sub> networks and often contain a portion of their tetrahedrally coordinated Si<sup>4+</sup> atoms isomorphously substituted for trivalent heteroatoms (e.g., Al<sup>3+</sup>), which give rise to anionic framework charges that are balanced by extraframework cations (e.g., H<sup>+</sup>

Received: September 14, 2020

Published: October 27, 2020



and  $\text{Na}^+$ ) and act as hydrophilic adsorption and catalytic active sites. Alternatively, siliceous zeolites may be synthesized with varied concentrations of framework defects to prepare hydrophilic<sup>14–17</sup> or hydrophobic<sup>17–19</sup> frameworks that contain a portion of their framework  $\text{Si}^{4+}$  atoms replaced by tetravalent Lewis acidic  $d^0$  (e.g.,  $\text{Ti}^{4+}$ ,  $\text{Zr}^{4+}$ , and  $\text{Hf}^{4+}$ ) or  $d^{10}$  (e.g.,  $\text{Sn}^{4+}$ ) transition metals with open coordination sites.<sup>18–22</sup> In these Lewis acid zeolites, hydrophilic defect sites (e.g., silanol groups) can form during crystallization when cationic structure directing agents are in excess of anionic framework charges, leading to the formation of charge balancing lattice  $\text{Si}-\text{O}^-$  defects,<sup>23,24</sup> or from the removal of framework heteroatoms (e.g., demetalation) to form silanol nests. Hydrophilic lattice defects formed during crystallization can be mitigated via the introduction of  $\text{F}^-$  anions to the synthesis media that incorporate during crystallization and balance excess cationic charge, giving rise to predominantly hydrophobic frameworks.<sup>25</sup>

The hydrophobicity of such microporous voids directly affects reaction kinetics in liquid media, for example, by altering the structure and dielectric properties of confined water relative to the bulk,<sup>26–33</sup> enabling selective adsorption of molecules from solutions based on polarity,<sup>34–41</sup> and by altering free energy barriers of reactions in liquid solvents.<sup>42,43</sup> Adsorption of pyridine from aqueous solution into siliceous MFI zeolites (293–353 K) shows more positive enthalpies and entropies of adsorption, relative to gas-phase pyridine adsorption, which were attributed to the more negative enthalpy and entropy of pyridine solvated in water compared to the gas phase.<sup>44,45</sup> Similarly, experimentally measured (368–383 K) and computed glucose adsorption entropies, which represent differences in entropy between glucose adsorbed within hydrophobic Beta zeolites and glucose in aqueous solution, are positive and likely reflect the unstructuring of first-shell water molecules that solvate glucose reactants and displacement of water molecules coordinated at the active site upon glucose adsorption within the zeolite pore.<sup>46,47</sup> In aluminosilicate zeolites, the density of hydrophilic binding sites (e.g.,  $\text{H}^+$  sites) confined within Beta zeolites alters phenol adsorption equilibrium constants in liquid water as hydrophobic voids more favorably adsorb phenol reactants and give rise to higher phenol alkylation turnover rates (523 K, per  $\text{H}^+$ ).<sup>48</sup> Additionally, both the density of  $\text{H}^+$  sites and framework connectivity have been shown to alter the extent that ethanol dehydration transition states perturb confined water structures in zeolites by influencing energetic penalties associated with solvent reorganization upon transition state formation.<sup>49</sup> In Lewis acidic zeolites, the preferential stabilization of inhibitory water–ethanol dimers at silanol ( $\text{SiOH}$ ) defects leads to lower apparent gas-phase ethanol dehydration turnover rates (404 K, per Sn) in hydrophilic than in hydrophobic Sn-Beta zeolites, despite similar intrinsic rate constants, because water–ethanol adducts are preferentially stabilized at hydrophilic binding sites and must be desorbed prior to formation of the transition state.<sup>50,51</sup> Hydrophobic  $\text{Ti}^{4+}$ - and  $\text{Sn}^{4+}$ -substituted Beta zeolites catalyze aqueous-phase glucose isomerization  $>10\times$  faster (per Lewis acid site, 373 K) than hydrophilic frameworks because hydrophobic voids inhibit the formation of extended water structures leading to lower activation free energy barriers.<sup>17,47,52,53</sup> Olefin epoxidation turnover rates (per Ti, 313–333 K) measured in nonaqueous solvents (e.g., methanol and acetonitrile) using aqueous  $\text{H}_2\text{O}_2$  as the oxidant, however, are larger in

hydrophilic Ti-zeolites (e.g., MFI and Beta) than in hydrophobic analogues,<sup>54–56</sup> which has been attributed to the preferential nucleation of water clusters at  $\text{SiOH}$  groups located near Lewis acidic Ti sites that lower the free energy barrier for the formation of the epoxidation transition state.<sup>54,57</sup> Collectively, these results highlight how water confined within hydrophobic and hydrophilic Lewis acidic zeolites influences catalysis for a variety of reactions, but the consequences of confined nonaqueous solvents, absent a cosolvent (e.g., water), on catalysis are not fully understood. The development of a mechanistic framework that describes the role of confined nonaqueous solvents will provide further insight into how microporous catalysts organize solvent and reactant molecules to modify reaction free energy landscapes during liquid-phase catalysis.

Here, we investigate how the polarity of the zeolite framework influences reaction rates in nonaqueous solvent systems in the context of the intermolecular Meerwein–Ponndorf–Verley reduction and Oppenauer oxidation (MPVO) transfer hydrogenation reaction between 2-butanol and cyclohexanone using hydrophobic Sn-Beta-F and hydrophilic Sn-Beta-OH zeolite catalysts. Turnover rates of intermolecular MPVO reactions have been recognized to depend on both the zeolite framework and solvent polarity,<sup>58,59</sup> but a more complete mechanistic understanding requires consideration of both reactant adsorption phenomena and the intrapore environment that solvates transition states. MPVO turnover rates (normalized per active site) are measured on Sn-Beta-F and Sn-Beta-OH as functions of temperature (333–393 K) and cyclohexanone activity and are used to extract enthalpic and entropic barriers that decouple cyclohexanone adsorption from transition state formation. Infrared spectra of adsorbed solvent molecules reveal that the polarity of the zeolite framework regulates the structure of the confined solvent, leading to differences in MPVO turnover rates that depend on the hydrophobic character of the zeolite framework. This set of spectroscopic and kinetic data reveals that these diverse solvent environments alter reactant adsorption thermodynamics that facilitate the partitioning of reactant and solvent molecules between the bulk and adsorbed phases. These findings provide mechanistic insight into how the structure of confined nonaqueous H-bonding solvent molecules alters the reaction and adsorption free energy landscape of MPVO catalysis and provides an extra dimension, beyond those aimed at modifying the active site directly, to tailor adsorption and catalytic phenomena in microporous materials.

## 2. EXPERIMENTAL METHODS

### 2.1. Synthesis of Siliceous and Sn-Containing Zeolites.

Hydrophobic Si-Beta (Si-Beta-F) and Sn-Beta (Sn-Beta-F) zeolites were crystallized via a direct hydrothermal route in the presence of  $\text{F}^-$  anions, which minimize the formation of framework defects in siliceous zeolites by balancing excess cationic charge during crystallization.<sup>25</sup> Specifically, Si-Beta-F was synthesized by the following procedure with a molar composition of 1  $\text{SiO}_2/0.54$  TEAOH/ $0.54$  HF/ $7.25$   $\text{H}_2\text{O}$ . An aqueous tetraethylammonium hydroxide solution (TEAOH; 23.38 g, Sigma-Aldrich, 40 wt %) was added to a perfluoroalkoxyalkane (PFA, Savillex Corp.) jar containing deionized water (18.2 M $\Omega$ -cm, 3.95 g) and stirred under ambient conditions for 5 min. Tetraethyl orthosilicate (TEOS; 25.00 g, Sigma-Aldrich, 99 wt %) was then added to the aqueous TEAOH solution, which was covered and stirred under ambient conditions for 2 h. The PFA jar was then uncovered, and ethanol and excess water were

**Table 1. Sn Content, Total Number of Lewis Acid Sites, Open/Closed Site Ratio, Total Number of SiOH Groups, and Absorption Edge Energy of Si-Beta-F, Si-Beta-OH, Sn-Beta-F, and Sn-Beta-OH Zeolites**

sample	Si Sn <sup>-1a</sup>	micropore volume <sup>b</sup>	LAS Sn <sup>-1c</sup>	open/closed ratio <sup>c</sup>	SiOH content <sup>c,d</sup>	edge energy <sup>e</sup>
Si-Beta-F		0.21			0.8	
Si-Beta-OH		0.18			33.9	
Sn-Beta-F	302	0.22	0.95	0.43	3.5	5.83
	264	0.19	0.86	0.56	4.9	
Sn-Beta-OH	326	0.19	0.74	0.74	63.0	5.63 (5.24) <sup>f</sup>
	412	0.19	0.68	0.48	52.1	
	553	0.20	0.71	0.47	51.4	

<sup>a</sup>Determined from ICP-MS. <sup>b</sup>Units of cm<sup>3</sup>/g at STP. Determined from N<sub>2</sub> adsorption isotherms measured at 77 K (section S2 of the Supporting Information). <sup>c</sup>Measured from IR spectra of adsorbed CD<sub>3</sub>CN (303 K; Figure 1, details in section S5 of the Supporting Information). <sup>d</sup>Units of 10<sup>-5</sup> mol of SiOH/g of zeolite. <sup>e</sup>Units of eV. Determined from intercepts of the linear portion of the adsorption edge (section S3 of the Supporting Information). <sup>f</sup>Absorption edge energy of low-energy shoulder listed in parentheses.

allowed to evaporate until the desired mass was obtained. Hydrofluoric acid (HF; 2.65 g, Sigma-Aldrich, 48 wt % in H<sub>2</sub>O, ≥99.99% trace metals basis) was then added dropwise, and the mixture was stirred with a PTFE spatula for 5 min. The mixture was then transferred to a 45 mL PTFE-lined, stainless steel autoclave (4744, Parr Instruments) and heated to 413 K under rotation (~40 rpm) for 7 days. Solids were recovered via centrifugation, washed with deionized water and acetone (99.5 wt %, BDH Chemicals) until the pH of the supernatant remained constant between washes, and dried overnight under ambient air at 393 K. The dried powder was then heated to 853 K (1 K min<sup>-1</sup>) under flowing dry air (100 cm<sup>3</sup> min<sup>-1</sup>; -80 °F dew point, Airgas) for 10 h.

Sn-Beta-F was prepared according to a previously reported procedure.<sup>58</sup> An aqueous TEAOH solution (11.65 g) was added to a PFA jar containing deionized water (8.44 g) and stirred under ambient conditions for 5 min. TEOS (12.10 g) was then added to the aqueous TEAOH solution, covered, and stirred under ambient conditions for 2 h. In a separate vessel, stannous chloride (Sn(II)Cl<sub>2</sub> · 2H<sub>2</sub>O; 0.044 g, Sigma-Aldrich, 98 wt %) was dissolved in ethanol (2 g, Koptec, 99.5 wt %) and added dropwise to the aqueous TEAOH and TEOS solution, which was then left uncovered and stirred under ambient conditions to evaporate ethanol and excess water. After the evaporation step, HF (1.30 g) was added dropwise, and the mixture was stirred with a PTFE spatula for 5 min. The resulting molar composition of the synthesis mixture was 1 SiO<sub>2</sub>/0.0033 SnO<sub>2</sub>/0.54 TEAOH/0.54 HF/7.52 H<sub>2</sub>O. Dealuminated Beta zeolite (0.173 g, 5 wt % SiO<sub>2</sub> basis) was added to the mixture, which was then transferred to a 45 mL PTFE lined, stainless steel autoclave and heated to 413 K under rotation (~40 rpm) for 7 days. Solids were then recovered via centrifugation, washed with deionized water and acetone until the pH of the supernatant remained constant between washes, and dried overnight under ambient air at 393 K. The dried powder was then heated to 853 K (1 K min<sup>-1</sup>) under flowing dry air (100 cm<sup>3</sup> min<sup>-1</sup>) for 10 h.

Dealuminated Beta (Si-Beta-OH; residual Si/Al > 5000) was prepared by addition of Al-Beta (1 g, Si/Al = 12.5, CP814E, Zeolyst) to concentrated nitric acid (HNO<sub>3</sub>; 80 g, 70 wt %, Sigma-Aldrich) in a PFA jar. The jar was sealed, heated to 353 K, and stirred for 24 h. After cooling to ambient temperature, the solids were recovered via centrifugation and washed repeatedly with deionized water until the pH between washes was constant. The solids were dried at 393 K overnight under ambient air and then heated to 853 K (1 K min<sup>-1</sup>) under flowing dry air (100 cm<sup>3</sup> min<sup>-1</sup>) for 10 h.

Sn-Beta-OH was synthesized via postsynthetic grafting of vacancy defects present in dealuminated Beta under dichloromethane reflux following reported procedures.<sup>14</sup> Dealuminated Beta zeolites (~1 g) and a PTFE stir bar were placed into a 500 cm<sup>3</sup> two-neck round-bottom flask. A septum stopper (Viton, Sigma-Aldrich) was used to seal one of the openings, and the other was connected to a Schlenk line via a reflux condenser. The dealuminated Beta zeolites were then dehydrated overnight at 473 K under dynamic vacuum (<1 Torr), cooled to room temperature, and then held under a dry N<sub>2</sub> purge

(liquid N<sub>2</sub> boil-off, Airgas). In a separate two-neck flask connected to the Schlenk line and sealed with a Viton septum, dichloromethane (DCM, 100 cm<sup>3</sup>, 99.8 wt %, Sigma-Aldrich) was dried on activated molecular sieves (dehydrated at 523 K overnight under vacuum; 3A, 4–8 mesh, Sigma-Aldrich) for 24 h under N<sub>2</sub> purge. Dried DCM (~25 cm<sup>3</sup>) was transferred to a sealed 50 cm<sup>3</sup> flask (Viton septum) via moisture-free cannula and transferred to a glovebox purged with dry N<sub>2</sub>, and the desired amount of an anhydrous 1 M stannic chloride in DCM solution (SnCl<sub>4</sub>, Sigma-Aldrich) was added to the sealed flask. The rest of the dried DCM and the SnCl<sub>4</sub> solution were then sequentially transferred to the flask containing the dealuminated Beta zeolites via moisture-free cannula and then stirred under DCM reflux (313 K) for 8 h. The solids were then recovered via centrifugation, washed repeatedly with methanol (35 cm<sup>3</sup> per wash), dried under ambient air overnight at 393 K, and then heated to 853 K (1 K min<sup>-1</sup>) under flowing dry air for 10 h.

Sn-xerogel was synthesized according to previously reported methods.<sup>52,60</sup> An aqueous 0.1 M hydrochloric acid solution (HCl; 2.81 g, 37 wt %, Sigma-Aldrich) was added to a PFA jar containing a solution of TEOS (25.2 g) and deionized water (34.7 g) and stirred for 2 h at ambient temperature. Next, tin(IV) chloride pentahydrate (SnCl<sub>4</sub> · 5H<sub>2</sub>O; 0.35 g, 98 wt %, Sigma-Aldrich) was added, and the mixture was stirred for 1 h. Finally, an aqueous 1 M ammonium hydroxide solution (NH<sub>4</sub>OH; 28–30 wt % NH<sub>3</sub> basis, Sigma-Aldrich) was added dropwise until the gel point was reached. The resulting gel was then dried at 433 K for 12 h, washed with deionized water until the pH remained constant between washes, dried at 373 K overnight, and then heated to 853 K (1 K min<sup>-1</sup>) under flowing dry air for 10 h.

Individual Sn-Beta samples will be referred to by using the following nomenclature to distinguish between different syntheses: Sn-Beta-X(Y), where X is either F (hydrophobic) or OH (hydrophilic) and Y is the Si/Sn molar ratio determined by ICP-MS.

**2.2. Catalyst Characterization.** Crystal structures of each Beta zeolite were determined from powder X-ray diffraction (XRD) patterns collected on a Bruker D8 diffractometer using Cu K $\alpha$  radiation (0.15406 nm) between 5° and 40° 2 $\theta$  and a scan rate of 0.077° s<sup>-1</sup>. XRD patterns of each Beta zeolite are shown in section S1 of the Supporting Information.

Nitrogen adsorption isotherms (77 K) were measured on a Quantachrome Autosorb iQ apparatus. All samples were pelleted and sieved to retain particulates between 150 and 250  $\mu$ m and degassed under vacuum (<5  $\mu$ mHg) for 12 h at 623 K prior to analysis. Micropore volumes were calculated by using a semilog derivative analysis of the isotherm ( $\partial(V_{\text{ads}}g^{-1})/\partial(\log(PP_0^{-1}))$  vs  $\log(PP_0^{-1})$ ), where the first minimum after the first maximum represents the end of micropore filling.<sup>61</sup> N<sub>2</sub> adsorption isotherms are shown in section S2 of the Supporting Information, and micropore volumes are tabulated in Table 1.

Diffuse reflectance ultraviolet–visible (DRUV) spectra were measured on a Cary 5000 spectrometer (Agilent) equipped with a DiffusIR diffuse reflectance accessory and environmental chamber (PIKE Technologies). Prior to measurement of a DRUV spectrum,

zeolite samples were dehydrated at 523 K ( $5 \text{ K min}^{-1}$ ) under flowing dry air for 2 h and then cooled to 298 K. All spectra of Sn-containing samples were measured relative to a dehydrated Si-Beta-F sample, and reflectance measurements were converted to absorbance by using the Kubelka–Munk function. DRUV spectra are shown in section S3 of the [Supporting Information](#).

Elemental analysis was performed by inductively coupled plasma mass spectrometry (ICP-MS) using an Agilent 7900 ICP-MS instrument. Zeolite powder ( $\sim 10 \text{ mg}$ ) was added to a polypropylene vial containing HF acid ( $200 \mu\text{L}$ ) and allowed to digest for 6 h prior to dilution with 2 wt %  $\text{HNO}_3$  (Veritas Double Distilled, GFS Chemicals Inc.) to obtain a predicted metal concentration of  $\sim 100$  ppb. Sn and Al concentrations were determined from calibration curves prepared from standard solutions of 1000 ppm of Sn in 10% hydrochloric acid (TraceCERT, Sigma-Aldrich) and 1000 ppm Al in 2%  $\text{HNO}_3$  (TraceCERT, Sigma-Aldrich), respectively, diluted in 2 wt %  $\text{HNO}_3$ .

**2.3. Measurement of IR Spectra.** IR spectra of adsorbed probe molecules were measured by using a Bruker Vertex 70 spectrometer equipped with a liquid  $\text{N}_2$  cooled Hg–Cd–Te (MCT) detector by averaging 128 scans at  $4 \text{ cm}^{-1}$  resolution between 4000 and  $400 \text{ cm}^{-1}$ . All IR spectra were collected relative to an empty cell spectrum measured at 303 K under dynamic vacuum ( $< 8.0 \times 10^{-5}$  Torr, Edwards T-Station 75 Turbopump). Zeolite powders ( $\sim 5\text{--}10 \text{ mg}$ ) were pressed into 7 mm diameter self-supporting wafers, secured in a sample holder (Harrick Scientific Products Inc.), and placed in a high-temperature transmission cell (Harrick Scientific Products Inc.) sealed with KBr windows ( $32 \times 3 \text{ mm}$ ; Harrick Scientific Products Inc.). The temperature of the sample was measured by a thermocouple (K-type, 1/16 in., Omega) inserted just below the sample holder and in contact with the internal cell wall and controlled by a Watlow EZ-Zone temperature controller. Both the cell inlet and outlet were connected to stainless steel bellows valves (SS-4BRG, Swagelok) to allow for isolation and evacuation of the transmission cell. The inlet valve was then connected via 1/4 in. flexible stainless-steel tubing (Swagelok) to a Schlenk line (Chemglass Airfree), which enabled isolation of the vacuum manifold, pretreatment gas manifold, and dosing ampules. The outlet valve was connected to an oil bubbler to monitor gas flow and minimize backflow of ambient air into the cell. Prior to collection of IR spectra, each sample was heated to 673 K ( $5 \text{ K min}^{-1}$ ) under flowing dry air ( $50 \text{ cm}^3 \text{ min}^{-1}$ ) for 2 h, cooled under flowing air to 303 K, and then evacuated until the pressure in the cell reached  $< 8.0 \times 10^{-5}$  Torr. IR spectra of clean Si and Sn-Beta zeolites, normalized by the total T–O–T overtone area ( $2100\text{--}1750 \text{ cm}^{-1}$ ), were measured under dynamic vacuum ( $< 8.0 \times 10^{-5}$  Torr) at 303 K after dehydration in dry air at 673 K and are shown in section S4 of the [Supporting Information](#).

Acetonitrile- $d_3$  ( $\text{CD}_3\text{CN}$ ; anhydrous,  $\geq 99.8$  atom % D, Sigma-Aldrich) and 2-butanol (99.8 wt %, Sigma-Aldrich) were purified via successive freeze–pump–thaw cycles to remove dissolved gases and volatiles and then introduced to the sample in serial doses ( $(1.4\text{--}7.0) \times 10^{-7}$  mol dose $^{-1}$ ). An IR spectrum was measured after each dose once the pressure in the cell remained constant for  $> 30$  s. The spectrum of the dehydrated parent zeolite was subtracted from all subsequent spectra after dosing, which were then baseline corrected and normalized by the total area of the T–O–T combination and overtones modes ( $2100\text{--}1750 \text{ cm}^{-1}$ ) of the parent zeolite sample. Assignments of  $\text{CD}_3\text{CN}$  coordinated to open Sn sites ( $\nu(\text{C}\equiv\text{N})$ :  $2316 \text{ cm}^{-1}$ ), closed Sn sites ( $2308 \text{ cm}^{-1}$ ), silanol groups ( $2275 \text{ cm}^{-1}$ ), and physisorbed or gas-phase  $\text{CD}_3\text{CN}$  ( $2265 \text{ cm}^{-1}$ ) are based on prior evidence.<sup>52,62,63</sup> The total number of SiOH groups, closed Sn sites, and open Sn sites were quantified from deconvolution of spectra at saturation into their principal components and using previously reported integrated molar extinction coefficients for  $\text{CD}_3\text{CN}$  adsorbed in Sn-Beta zeolites (details in section S5 of the [Supporting Information](#)).<sup>52</sup> 2-Butanol used in dosing experiments was purified by refluxing over sodium borohydride ( $\text{NaBH}_4$ ,  $> 95\%$ , Macron Fine Chemicals) for 12 h and then distilled to remove residual carbonyl impurities (see section S6 of the [Supporting Information](#)).<sup>64</sup>

**2.4. Measurement of MPVO Kinetics.** MPVO kinetic studies were performed in glass batch reactors ( $10 \text{ cm}^3$ , VWR Scientific) using reactant solutions containing 0.01–1 M cyclohexanone (99.5 wt %, Sigma-Aldrich) in a bulk 2-butanol (99.8 wt %, Sigma-Aldrich) solvent. Prior to rate measurements, glass batch reactors were sonicated for a minimum of 15 min in acetone, isopropanol (99.5 wt %, VWR), and deionized water, dried at 393 K, and flushed with dry  $\text{N}_2$  after cooling to room temperature. Zeolite powder ( $\sim 5\text{--}10 \text{ mg}$ ) and a PTFE-coated magnetic stir bar were loaded into a glass batch reactor and sealed with a PTFE-faced silicone septum housed in an aluminum crimp top (Supelco). The reactant solution ( $\sim 2 \text{ cm}^3$ ) was added to a separate glass batch reactor and sealed, and both catalyst and reactant vials were heated to the desired reaction temperature ( $333\text{--}393 \text{ K}$ ) for  $> 15$  min to minimize thermal gradients at initial reaction times. The molar ratio of cyclohexanone to total Sn in the reaction was maintained at  $> 100$  for all rate measurements. After preheating, the reactant solution was transferred to the catalyst vial via gastight syringe, and the reaction allowed to proceed under stirring (300 rpm) for  $\sim 5$  min ( $> 373 \text{ K}$ ), 10 min ( $373 \text{ K}$ ), or 20 min ( $< 373 \text{ K}$ ). The catalytic reaction mixture was then quenched in an ice bath, filtered through a  $0.2 \mu\text{m}$  PTFE syringe filter (VWR), and diluted with a 2-pentanone standard solution (5 wt % in 2-butanol; 99.5 wt %, HPLC grade, Sigma-Aldrich). Filtered reaction solutions were then injected into a gas chromatograph (7890A, Agilent Technologies) equipped with a DB-1701 column ( $30 \text{ m} \times 250 \mu\text{m} \times 0.25 \mu\text{m}$ , Agilent) and a flame ionization detector. Initial MPVO turnover rates (normalized per open Sn site) were calculated by extrapolation of the total cyclohexanol production (moles of cyclohexanol produced per open Sn site) to zero reaction time (i.e., zero conversion). This single point method yielded kinetic data measured at  $< 5\%$  conversion for all reaction conditions investigated and gave similar initial rates (within 20%) to those calculated from full transient reaction profiles (details in section S8 of the [Supporting Information](#)).

### 3. RESULTS AND DISCUSSION

**3.1. Quantification of Active Sn Sites and SiOH Groups in Sn-Beta.** Mechanistic interpretation of kinetic data measured on Sn-Beta zeolites with different pore polarity requires that turnover rates are rigorously normalized by the total number of active sites that catalyze such reactions. Sn-Beta zeolites contain at least two distinct framework Sn coordination environments: closed Sn sites with 4-fold coordination to lattice O atoms ( $(\text{SiO})_4\text{Sn}$ ) or open Sn sites with 3-fold coordination to lattice O atoms and a hydroxide ligand ( $(\text{SiO})_3\text{SnOH}$ ). These different Sn coordination environments have been identified by using a combination of various computational<sup>50,63,65–67</sup> and experimental<sup>51,52,62,63,67–69</sup> methods and differ in their ability to activate C–O bonds.<sup>50–52,58,63</sup> Specifically, both inter- and intramolecular MPVO reactions are catalyzed by open Sn sites in Sn-Beta zeolites.<sup>52,58,63,67,70</sup> IR spectra of adsorbed deuterated acetonitrile- $d_3$  ( $\text{CD}_3\text{CN}$ ) can differentiate between these different Sn sites because the electron density of the nitrile bond is perturbed to different extents upon ligation to open or closed Sn sites.<sup>52,63</sup>  $\text{CD}_3\text{CN}$  preferentially coordinates to open Sn sites ( $\nu(\text{C}\equiv\text{N})$ :  $2315 \text{ cm}^{-1}$ ) in Sn-Beta at low coverages, prior to adsorption at closed Sn sites ( $\nu(\text{C}\equiv\text{N})$ :  $2308 \text{ cm}^{-1}$ ), which is characterized by a red-shift in the peak center of Lewis acid bound  $\text{CD}_3\text{CN}$  (Figure 1) and consistent with prior observations for  $\text{CD}_3\text{CN}$  adsorbed on Sn-zeolites.<sup>52</sup> At increasing coverages, vibrational bands reflecting  $\text{CD}_3\text{CN}$  adsorbed at SiOH groups ( $\nu(\text{C}\equiv\text{N})$ :  $2275 \text{ cm}^{-1}$ ) and physisorbed or gas-like  $\text{CD}_3\text{CN}$  ( $\nu(\text{C}\equiv\text{N})$ :  $2265 \text{ cm}^{-1}$ ) are also observed. All Sn-Beta-F and Sn-Beta-OH zeolites exhibit substoichiometric fractions of Sn present as Lewis acid sites ( $\text{LAS}/\text{Sn} = 0.68\text{--}0.95$ ), in agreement with UV–vis spectra

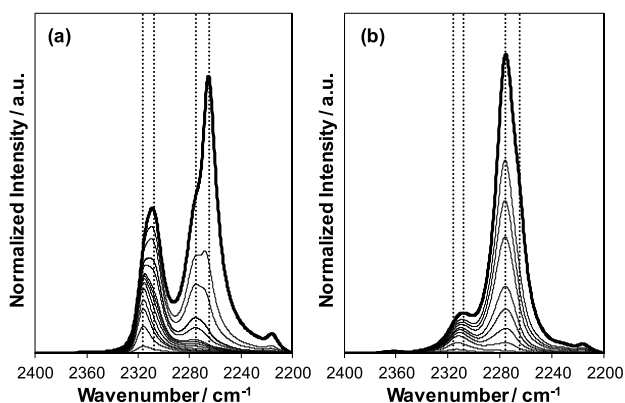


**Figure 1.** IR difference spectra (relative to the parent spectrum) of (a) Sn-Beta-F(302) and (b) Sn-Beta-OH(326) with increasing coverage of  $\text{CD}_3\text{CN}$  measured at 303 K. Dashed lines indicate expected  $\nu(\text{C}\equiv\text{N})$  stretching frequencies for  $\text{CD}_3\text{CN}$  coordinated to open Sn sites ( $2315\text{ cm}^{-1}$ ), closed Sn sites ( $2308\text{ cm}^{-1}$ ), and SiOH groups ( $2275\text{ cm}^{-1}$ ) and for physisorbed or gas-phase  $\text{CD}_3\text{CN}$  ( $2265\text{ cm}^{-1}$ ).

that indicate a small fraction of  $\text{SnO}_x$  is present on these zeolites (section S3 of the Supporting Information) and ratios of open to closed Sn sites (Table 1) that are similar to those expected for Sn-Beta (open/closed = 0.44–0.74).<sup>52</sup>

Adsorbed  $\text{CD}_3\text{CN}$  also enables quantitative titration of the total number of SiOH groups present in Lewis acidic Beta zeolites,<sup>47,52</sup> which provides a comparative metric for the total number of hydrophilic binding sites present in Sn-Beta-F and Sn-Beta-OH. These titration data show that Sn-Beta-OH zeolites contain  $>10\times$  more SiOH groups than Sn-Beta-F (Table 1), similar to the difference between purely siliceous Si-Beta-F and Si-Beta-OH zeolites (Table 1; spectra shown in section S5 of the Supporting Information). The difference in hydrophobicity between these different classes of Sn-Beta catalysts was confirmed by measurement of first-order glucose isomerization rate constants in liquid water (373 K, per open Sn site) that are  $\sim 16\times$  larger on Sn-Beta-F(302) than on Sn-Beta-OH(326) (details in section S7 of the Supporting Information). These results are consistent with previous reports for glucose-to-fructose isomerization in hydrophobic and hydrophilic Sn-Beta zeolites<sup>14,52</sup> and arise because hydrophobic voids exclude bulk water structures leading to lower free energy barriers for the formation of the isomerization transition state.<sup>17,47,52</sup> Collectively, these data indicate that Sn-Beta-F and Sn-Beta-OH contain a similar fraction of Lewis acidic Sn sites but differ drastically in framework polarity as determined by titration of SiOH groups by  $\text{CD}_3\text{CN}$  (Table 1 and Figure 1) and measurement of glucose isomerization first-order rate constants (373 K, per open Sn; section S7 of the Supporting Information).

**3.2. Kinetics and Mechanism of MPVO Reactions Catalyzed by Sn-Beta Zeolites.** MPVO kinetic data measured on Sn-Beta zeolites are not influenced by background reactions in the homogeneous phase or those that might be catalyzed by  $\text{SnO}_2$  domains and were determined to be free of internal mass transport artifacts under the conditions investigated here (details in section S8 of the Supporting Information). Initial turnover rates of the MPVO reaction between 2-butanol and cyclohexanone were measured on Sn-Beta-F(302) and Sn-Beta-OH(326) zeolites as a function of cyclohexanone concentration (0.01–1 M) and temperature

(333–393 K) in a 2-butanol solvent. Thermodynamic activities of cyclohexanone and 2-butanol are used to describe initial MPVO turnover rates instead of concentration due to expected nonideal solution behavior that affect reaction rates.<sup>71</sup> Temperature- and concentration-dependent solution phase activity coefficients ( $\gamma_i$ ) were estimated by using the UNIFAC group contribution method,<sup>72–74</sup> and the activity of each species ( $a_i$ ) was calculated via the following equation:

$$a_i = \gamma_i \left( \frac{C_i}{C_i^0} \right) \quad (1)$$

where  $C_i$  is the concentration ( $\text{mol L}^{-1}$ ) of species  $i$  in solution and  $C_i^0$  is the standard state concentration equal to the concentration ( $\text{mol L}^{-1}$ ) of the pure component, such that the activity of the pure species equals unity.

Initial MPVO turnover rates (normalized per open Sn site) measured as a function of cyclohexanone activity ( $a_c$ ; 0.01–1 M cyclohexanone) and temperature (333–393 K) in 2-butanol on Sn-Beta-F(302) and Sn-Beta-OH(326) show a first-order dependence on cyclohexanone activity at low values of  $a_c$ , consistent with previous MPVO kinetic studies performed at low ketone concentrations in an alcohol solvent on Lewis acidic Beta zeolites,<sup>58</sup> and transition to a zero-order kinetic regime at higher values of  $a_c$  (Figure 2). Initial MPVO

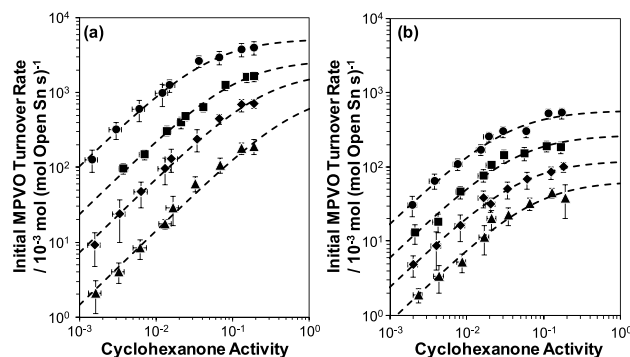


**Figure 2.** Cyclohexanol formation rates (per open Sn site) measured on (a) Sn-Beta-F(302) and (b) Sn-Beta-OH(326) as a function of cyclohexanone activity (0.01–1 M cyclohexanone) in 2-butanol at 333 K (triangles), 353 K (diamonds), 373 K (squares), and 393 K (circles). Dashed lines are regressions of eq 5. Error bars are determined from propagation of experimental uncertainty.

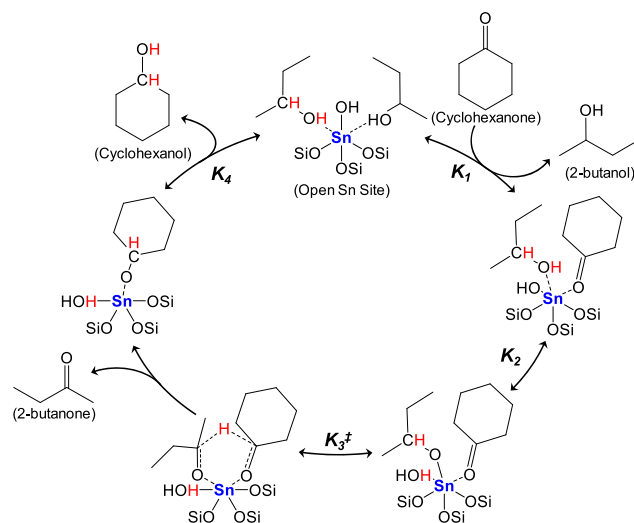
turnover rates (per open Sn site) are similar (within  $2\times$ ) on both Sn-Beta-F(302) and Sn-Beta-OH(326) at low temperatures ( $<353\text{ K}$ ) and low values of  $a_c$  ( $<10^{-2}$ ) but deviate with increasing values of  $a_c$  and temperature and are 5– $10\times$  higher on hydrophobic Sn-Beta-F than on hydrophilic Sn-Beta-OH in the zero-order regime across all temperatures ( $a_c > 10^{-1}$ ; Figure 2). These differences in initial MPVO turnover rate at high ketone concentration are consistent with prior reports that rates of MPVO between 4-*tert*-butylcyclohexanone in a 2-propanol solvent (355 K, per total Zr; 1 M 4-*tert*-butylcyclohexanone) are larger in Zr-Beta zeolites synthesized in  $\text{F}^-$  media ( $522\text{ h}^{-1}$ ) than those prepared via postsynthetic grafting of dealuminated Beta with  $\text{Zr}(\text{NO}_3)_4$  or  $\text{ZrOCl}_2$  ( $20\text{--}350\text{ h}^{-1}$ ).<sup>59</sup> Additionally, the differences in initial MPVO turnover rate (per open Sn) between hydrophobic and hydrophilic Sn-Beta catalysts that manifest at different temperatures and cyclohexanone activities are likely not a result of trace water

present in the reaction media, which is known to inhibit homogeneous metal–alkoxide MPV reduction catalysts.<sup>75</sup> Initial MPVO turnover rates (0.01–1 M cyclohexanone in 2-butanol, 373 K, per open Sn) measured under anhydrous conditions on Sn-Beta-F and Sn-Beta-OH catalysts are similar (within 1.5×) to those measured under standard reaction conditions (~2–3 wt % H<sub>2</sub>O under an ambient atmosphere; details in section S8 of the Supporting Information), further emphasizing the water tolerance of isolated Lewis acidic metal centers hosted in microporous siliceous frameworks. Thus, we propose that the observed transition from a first-order to zero-order kinetic regime with increasing  $a_c$  is consistent with a change in the most abundant reactive intermediate (MARI) from a solvent-covered active site to one involving cyclohexanone adsorbed at the active site. Interestingly, the onset of the zero-order kinetic regime on Sn-Beta-F(302) occurs at nearly a 10× lower value of  $a_c$  at 393 K than at 333 K (Figure 2), a phenomenon not observed on Sn-Beta-OH(326), suggesting that the coverage of kinetically relevant intermediates on Sn-Beta-F(302), but not Sn-Beta-OH(326), is strongly dependent on both  $a_c$  and temperature. These results indicate that initial MPVO turnover rates (per open Sn site) depend on the polarity of the zeolite framework, and this effect is further examined by using transition state theory.

Intermolecular MPVO reactions between an alcohol and a ketone occur via the same mechanism, regardless of alcohol or ketone identity, on both homogeneous<sup>76,77</sup> and heterogeneous<sup>58,78,79</sup> Lewis acid catalysts. In a 2-butanol solvent, the MPVO reaction between 2-butanol and cyclohexanone on Sn-Beta proceeds over a 2-butanol-covered open Sn site via quasi-equilibrated adsorption of cyclohexanone, liberating an adsorbed 2-butanol molecule and forming a coadsorbed 2-butanol–cyclohexanone adduct (step 1, Scheme 1). 2-Butanol then undergoes quasi-equilibrated deprotonation with the stannanol group to form an adsorbed 2-butoxide species and water,<sup>58,79,80</sup> which remains coordinated to the Sn site (step 2, Scheme 1). The coadsorbed 2-butoxide–cyclohexanone precursor then proceeds through the rate-controlling C-1 hydride shift transition state to form 2-butanone and an adsorbed cyclohexoxide (step 3, Scheme 1). Formation of the hydride shift transition state in Lewis acidic zeolites has been shown to be the rate-controlling step from density functional theory (DFT) calculated reaction barriers for the MPVO reaction between 2-butanol and cyclohexanone<sup>79</sup> and experimentally measured kinetic isotope effects between methyl levulinate and deuterated 2-propanol (423 K, labeling confirmed by <sup>1</sup>H NMR).<sup>58</sup> The cyclohexoxide ligand is then protonated via water decomposition to form cyclohexanol and regenerate the open Sn site (step 4, Scheme 1). Considering the formation of the hydride shift transition state as the rate-controlling step and the observed change in the MARI from a likely 2-butanol-covered open Sn site to a coadsorbed 2-butanol–cyclohexanone adduct with increasing cyclohexanone activity (Figure 2), a rate expression can be derived by using transition state theory which describes the kinetic dependence of initial MPVO turnover rates on cyclohexanone activity (full derivation in section S9 of the Supporting Information):

$$\frac{r_{\text{net}}}{[L]} = \frac{\gamma_{A^*} K_1 K_2 k_3 a_C}{\gamma_{BB^*} a_B + K_1 a_C} (1 - \eta) \quad (2)$$

**Scheme 1.** Proposed MPVO Reaction Mechanism between 2-Butanol and Cyclohexanone over an Open Sn Site in a 2-Butanol Solvent<sup>a</sup>



<sup>a</sup>Quasi-equilibrated adsorption of cyclohexanone displaces an adsorbed 2-butanol molecule from the open Sn site (step 1) and precedes the deprotonation of 2-butanol to form an adsorbed 2-butoxide (step 2). This step is followed by the formation of the rate-controlling hydride shift transition state to form 2-butanone and an adsorbed cyclohexoxide (step 3), which is then protonated to form cyclohexanol and desorbs to return the 2-butanol-covered open Sn site (step 4).

Here,  $K_j$  represents the equilibrium constant of step  $j$ ,  $k_3$  is the intrinsic rate constant,  $a_C$  and  $a_B$  are the solution phase thermodynamic activities (described by eq 1) of cyclohexanone and 2-butanol, respectively,  $\gamma_{\ddagger}$  is the activity coefficient of the transition state,  $\gamma_{A^*}$  is the activity coefficient of the coadsorbed 2-butanol–cyclohexanone adduct,  $\gamma_{BB^*}$  is the activity coefficient of the 2-butanol-covered open Sn site,  $\eta$  is the approach to equilibrium, and  $[L]$  is the number of open Sn sites (i.e., active sites). Given the low concentration of Sn sites present in the Sn-Beta catalysts used in this study (Si/Sn = 250–550; <1 Sn atom per 4 unit cells) and assuming that the intraporous solvating environment does not change substantially with increasing cyclohexanone activity, adsorbed intermediates reflect ideal noninteracting species and satisfy the basic assumptions of the idealized Langmuir adsorption model. Thus, we make the approximation that the activity coefficients of all adsorbed species and transition states are unity under the conditions studied here:

$$\frac{r_{\text{net}}}{[L]} = \frac{K_1 K_2 k_3 a_C}{a_B + K_1 a_C} (1 - \eta) \quad (3)$$

MPVO turnover rates are reported as initial turnover rates extrapolated to zero conversion, which causes  $\eta$  to approach zero (i.e.,  $X \rightarrow 0$ ,  $\eta \rightarrow 0$ ), resulting in eq 4 which describes MPVO turnover rates at initial time:

$$\frac{r_{\text{net}}}{[L]} = \frac{K_1 K_2 k_3 a_C}{a_B + K_1 a_C} \quad (4)$$

It should be noted that the activity of 2-butanol in the bulk solution,  $a_B$ , does decrease systematically ( $a_B = 0.999$ – $0.900$ ) with increasing cyclohexanone activity in solution, and this change in activity of solution-phase 2-butanol is explicitly

accounted for in eq 4. The individual contributions from  $K_2$  and  $k_3$  to the free energy barrier of reaction cannot be uniquely decoupled from experimental kinetic measurements alone and are thus lumped together into an apparent zero-order rate constant ( $k_{app}$ ) that reflects the difference in free energy between the hydride shift transition state ( $\ddagger$ ) and the coadsorbed 2-butanol–cyclohexanone adduct ( $A^*$ ):

$$\frac{r_{net}}{[L]} = \frac{K_{ads}k_{app}a_c}{a_B + K_{ads}a_c} \quad (5)$$

This equation provides a mechanistic basis to interpret how zeolite hydrophobicity influences initial MPVO turnover rates and the coverage of kinetically relevant intermediates.

Apparent zero-order MPVO rate constants ( $k_{app}$ , normalized per open Sn site) are  $\sim 10\times$  larger on hydrophobic Sn-Beta-F(302) than on Sn-Beta-OH(326) at all studied reaction temperatures (333–393 K; Figure 3). These data indicate that

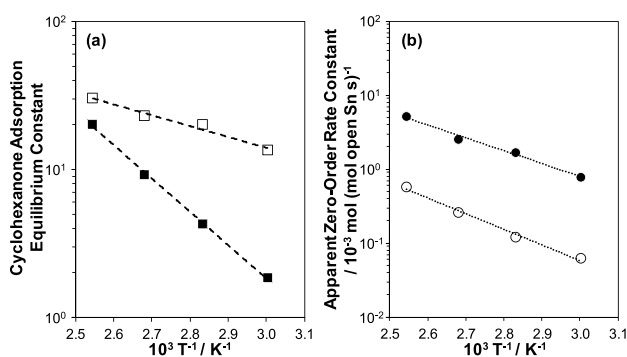


**Figure 3.** Cyclohexanone adsorption equilibrium constants (a;  $K_{ads}$ ) and apparent zero-order rate constants (b;  $k_{app}$ , per open Sn site) determined by regression of eq 5 to initial MPVO turnover rates (per open Sn site, Figure 2) measured on Sn-Beta-F(302) (filled) and Sn-Beta-OH(326) (open) in a 2-butanol solvent as a function of temperature (333–393 K). Dashed lines are exponential fits to the data.

the intraporous solvating environment within hydrophobic Sn-Beta-F zeolites gives rise to lower apparent zero-order MPVO free energy barriers (which relate differences in the free energy between the hydride shift transition state and the coadsorbed 2-butanol–cyclohexanone adduct) when compared to those of hydrophilic Sn-Beta-OH zeolites despite both materials having open Sn sites that catalyze the same set of MPVO elementary steps. Cyclohexanone adsorption equilibrium constants ( $K_{ads}$ ) increase with increasing temperature on both Sn-Beta-F(302) and Sn-Beta-OH(326), indicating that cyclohexanone adsorption from the solution to the open Sn site becomes *more* favorable with increasing temperature in both Sn-Beta catalysts. The value of  $K_{ads}$  measured on hydrophobic Sn-Beta-F, however, is more sensitive to changes in temperature than that measured on Sn-Beta-OH ( $\sim 10\times$  change on Sn-Beta-F,  $\sim 2.5\times$  on Sn-Beta-OH; 333–393 K), suggesting that different intraporous solvating environments are likely present within the microporous voids of hydrophobic and hydrophilic Sn-Beta zeolites, as changes in adsorption free energies of cyclohexanone within the same zeolite framework are referenced to an identical solution phase.

Initial MPVO turnover rates vary continuously from first- to zero-order with increasing values of  $a_c$  on Sn-Beta catalysts, but the onset of the zero-order kinetic regime, and thus the

coverage of adsorbed cyclohexanone adducts, shows different dependencies on cyclohexanone activity at different temperatures on Sn-Beta-F(302) and Sn-Beta-OH(326) zeolites (Figure 2). The rate equation given by eq 5 provides a mechanistic basis for this transition between first- and zero-order kinetic regimes and enables the estimation of surface coverages during MPVO catalysis.<sup>81,82</sup> A relationship between the apparent cyclohexanone reaction order ( $\Psi_c$ ) and the fractional coverage of cyclohexanone within Sn-Beta zeolites ( $\theta_c$ , per open Sn site) can be determined by differentiating the natural log of the MPVO rate equation (eq 5) with respect to the natural log of the cyclohexanone activity ( $a_c$ ):

$$\Psi_c = \frac{\partial \ln(r)}{\partial \ln(a_c)} = 1 - \frac{K_{ads}a_c}{a_B + K_{ads}a_c} = 1 - \theta_c \quad (6)$$

where  $\frac{K_{ads}a_c}{a_B + K_{ads}a_c}$  is the fractional coverage of cyclohexanone ( $\theta_c$ ) described by the Langmuir adsorption isotherm and, assuming ideal adsorption behavior, leads to the following relationship between the MPVO turnover rate and the fractional coverage of cyclohexanone:

$$\theta_c = 1 - \frac{\partial \ln(r)}{\partial \ln(a_c)} \quad (7)$$

Figure 4 shows  $\theta_c$  calculated as a function of cyclohexanone activity and temperature on both Sn-Beta-F(302) and Sn-Beta-

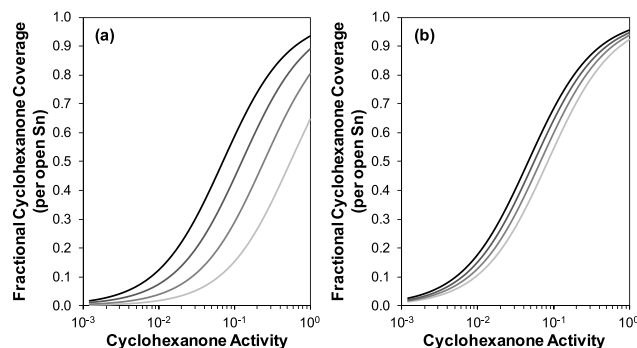


**Figure 4.** Fractional cyclohexanone coverage (per open Sn site) calculated from eq 7 as a function of temperature (333–393 K light to dark) and cyclohexanone activity (0.01–1 M cyclohexanone) in a 2-butanol solvent on (a) Sn-Beta-F(302) and (b) Sn-Beta-OH(326).

OH(264). The origin of the strong temperature dependence of the shift in kinetic regime observed on Sn-Beta-F(302) can be rationalized by the 5–6 $\times$  larger cyclohexanone coverage expected at 393 K than 333 K at low values of cyclohexanone activity ( $a_c < 0.1$ ), suggesting that cyclohexanone adsorption becomes preferred at elevated temperatures in hydrophobic Sn-Beta-F zeolites. The fractional coverage of cyclohexanone predicted on Sn-Beta-OH shows a less dramatic increase with temperature at low values of cyclohexanone activity ( $\sim 1.5\times$  between 393 and 333 K at  $a_c < 0.1$ ). The greater insensitivity of  $\theta_c$  to changes in reaction temperature on Sn-Beta-OH, relative to Sn-Beta-F, suggests that the solvating environment confined within hydrophilic Sn-Beta-OH is more similar to that of the solution phase and differs from that confined within hydrophobic Sn-Beta-F. On the basis of these observations, we hypothesize that hydrophobic zeolites induce structural ordering on confined hydrogen-bonded (H-bonded) 2-butanol networks, similar to how H-bonding water networks become

ordered when confined within subnanometer hydrophobic voids. Conversely, 2-butanol adsorbed within a hydrophilic zeolite would be expected to adopt a more disordered, liquidlike structure due to favorable H-bonding interactions between framework SiOH defects and adsorbed 2-butanol molecules.

**3.3. IR Spectra of 2-Butanol Adsorbed on Sn-Beta Zeolites of Different Polarity.** The difference in the structure of adsorbed 2-butanol within hydrophobic and hydrophilic Sn-Beta zeolites was probed by measuring IR spectra of Sn-Beta-F(302) and Sn-Beta-OH(326) zeolites in equilibrium with various pressures of 2-butanol. Figure 5a

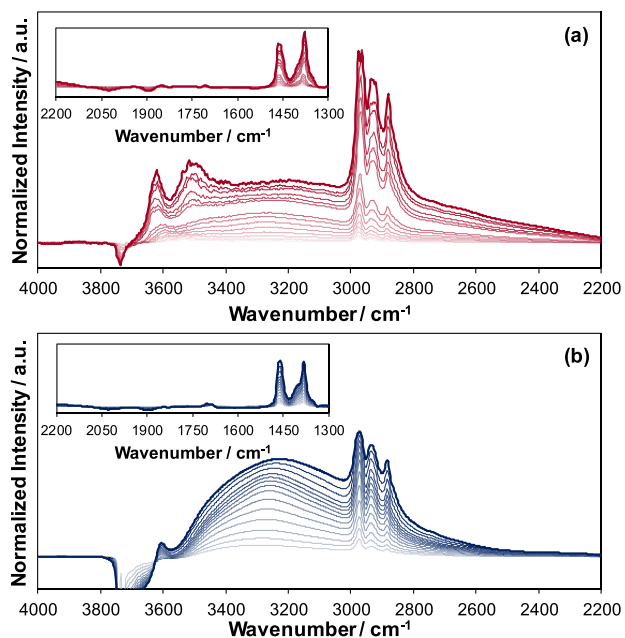


**Figure 5.** IR difference spectra (relative to the parent spectrum) of (a) Sn-Beta-F(302) and (b) Sn-Beta-OH(326) with increasing equilibrium pressure of 2-butanol (light to dark) measured at 303 K. Insets show the region from 2200 to 1300  $\text{cm}^{-1}$ .

shows IR spectra of 2-butanol adsorbed on Sn-Beta-F(302), after subtraction and normalization by the total T–O–T overtone area (2100–1750  $\text{cm}^{-1}$ ) of the parent zeolite, measured with increasing 2-butanol partial pressure at 303 K (spectra of 2-butanol adsorption on Si-Beta zeolites are shown in section S6 of the Supporting Information). Features characteristic of adsorbed 2-butanol monomers are observed at low equilibrium pressures of 2-butanol and are characterized by the appearance of an O–H stretching feature centered near 3600  $\text{cm}^{-1}$ , which is similar to that of gas-phase 2-butanol<sup>83</sup> and spectral features observed when low concentrations of alcohols are adsorbed in nonpolar solvents,<sup>84–88</sup> suggesting the presence of isolated 2-butanol molecules. Concurrent to the formation of 2-butanol monomers at low dosing pressures, a decrease in the OH stretching mode of isolated SiOH groups ( $\sim 3700 \text{ cm}^{-1}$ ) is observed that is accompanied by the appearance of symmetric and asymmetric C–H stretching modes of the various  $\text{CH}_x$  groups (3000–2800  $\text{cm}^{-1}$ ) and C–H and O–H bending modes (1500–1350  $\text{cm}^{-1}$ ). A broad feature centered near  $\sim 3300 \text{ cm}^{-1}$  also forms at low 2-butanol pressures and is attributed to a combination of perturbed SiOH and 2-butanol OH groups,<sup>87–91</sup> which are absent at low

coverages of 2-butanol on Si-Beta-F (section S6 of the Supporting Information). The signals assigned to perturbed OH groups likely represent the preferential adsorption of 2-butanol at framework Sn sites and SiOH defects that are observed on the dehydrated parent Sn-Beta-F(302) zeolite (spectra in section S4 of the Supporting Information).

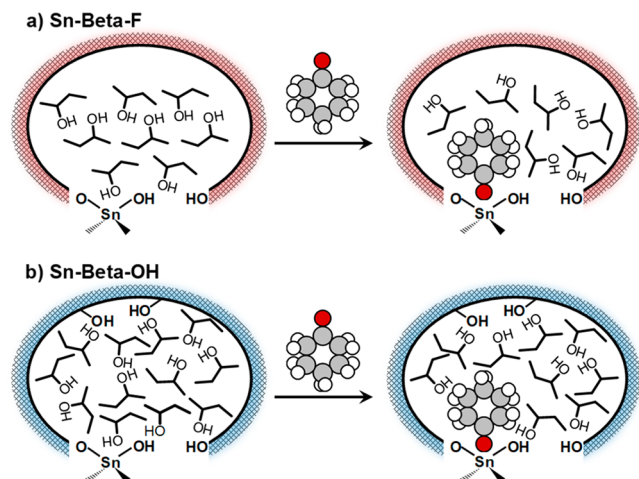
These data are consistent with the preferential adsorption and nucleation of small water or alcohol clusters at hydrophilic binding sites (e.g., metal heteroatoms, SiOH defects, or  $\text{H}^+$  sites) confined within zeolites prior to the formation of extended solvent structures.<sup>28,49,92,93</sup> Increasing the equilibrium coverage of 2-butanol results in stronger 2-butanol monomer peak intensities and is accompanied by a blue-shift (toward 3620  $\text{cm}^{-1}$ ) and sharpening of this feature. This phenomenon likely reflects the adsorption of 2-butanol monomers within a less polar intraporous solvating environment due to the absence of coadsorbed 2-butanol molecules that modify the local electric field near the OH dipole.<sup>94–97</sup> The vibrational peak characteristic of 2-butanol monomers undergoes a red-shift with increasing 2-butanol coverage in hydrophobic Si-Beta-F (3635 to 3609  $\text{cm}^{-1}$ , section S6 of the Supporting Information), suggesting that the intraporous solvating environment becomes more polar as increasing amounts of 2-butanol are adsorbed within the purely siliceous pores of Si-Beta-F. These results suggest that 2-butanol preferentially adsorbs at hydrophilic Sn sites (or at the minority SiOH defect sites) prior to adsorption within the extended hydrophobic channel environment that bridge Sn sites confined in Sn-Beta-F zeolites. At the highest equilibrium 2-butanol coverages, a new feature centered at  $\sim 3510 \text{ cm}^{-1}$  appears and grows with 2-butanol pressure—an effect that is reminiscent of the formation of H-bonded alcohol dimers observed from IR spectra of light alcohols ( $\text{C}_1\text{–C}_4$ ) dissolved in nonpolar solvents (3540–3500  $\text{cm}^{-1}$ ).<sup>86–89</sup>

Adsorption of 2-butanol at low pressures within hydrophilic Sn-Beta-OH (Figure 5b) and Si-Beta-OH (section S6 of the Supporting Information), however, occurs via H-bonding to SiOH groups as evidenced by the decrease in intensity of various SiOH groups ( $\sim 3740\text{–}3650 \text{ cm}^{-1}$ ; nests and isolated SiOH) and coincident formation of a broad peak centered near 3300  $\text{cm}^{-1}$ , characteristic of perturbed OH stretching modes, that increases in intensity with increasing 2-butanol adsorption. C–H stretching modes (3000–2800  $\text{cm}^{-1}$ ) and C–H and O–H bending modes (1500–1350  $\text{cm}^{-1}$ ) that increase in intensity with increasing 2-butanol partial pressure are also observed. The broad absorption feature between 3700 and 3000  $\text{cm}^{-1}$  was qualitatively deconvoluted into four component peaks (section S6 of the Supporting Information), corresponding to 2-butanol monomers (3611  $\text{cm}^{-1}$ ), 2-butanol dimers (3480  $\text{cm}^{-1}$ ), polymeric 2-butanol networks (3393  $\text{cm}^{-1}$ ), and perturbed SiOH groups (3240  $\text{cm}^{-1}$ ) to better identify component peaks in this absorption region. As the 2-butanol partial pressure increases, a peak attributed to monomeric 2-butanol appears near 3610  $\text{cm}^{-1}$  and, unlike in Sn-Beta-F, does not red-shift with increasing 2-butanol adsorption, suggesting that 2-butanol monomers experience a similar solvating environment within the zeolite pore that is independent of the amount of 2-butanol adsorbed. The peak attributed to perturbed SiOH groups ( $\sim 3300 \text{ cm}^{-1}$ ) increases in intensity and red-shifts with increasing adsorption of 2-butanol indicative of increasing extents of H-bonding between SiOH and 2-butanol at higher coverages.<sup>95,98</sup> At intermediate 2-butanol coverages a shoulder appears near 3480  $\text{cm}^{-1}$  that is

attributed to 2-butanol dimers and precedes the formation of oligomeric 2-butanol clusters, which give rise to a feature centered near 3393  $\text{cm}^{-1}$  at high 2-butanol pressures that resembles liquidlike alcohols.<sup>87–91</sup> This data set indicates that the presence of H-bonding groups (e.g., SiOH defects) allows adsorbed 2-butanol molecules to adopt a disordered, liquidlike network of H-bonds within hydrophilic Sn-Beta-OH zeolites that resembles bulk 2-butanol.

In contrast, the pores of hydrophobic Sn-Beta-F appear to impede the formation of liquidlike 2-butanol oligomers and instead give rise to primarily dimeric 2-butanol species near pore-filling that we speculate adopt a similar pseudo one-dimensional wirelike structure to that observed for water confined within subnanometer hydrophobic pores (diameter <1 nm).<sup>28,29,99–103</sup> These dipole-oriented ordered water networks confined within the hydrophobic voids of zeolites also appear in biological catalysts and give rise to positive entropies of reactant adsorption and transition state formation due to reorganization and displacement of confined solvent molecules.<sup>1–4,104,105</sup> We hypothesize that the ordered 2-butanol networks confined within Sn-Beta-F are disrupted to a greater extent than the liquidlike networks observed within Sn-Beta-OH, giving rise to entropically driven adsorption of cyclohexanone due to the need to liberate an ordered H-bonding network (Scheme 2) and results in more favorable

**Scheme 2. Adsorption of Cyclohexanone within the 2-Butanol Filled Pores of (a) Hydrophobic Sn-Beta-F and (b) Hydrophilic Sn-Beta-OH<sup>a</sup>**



<sup>a</sup>Atom color codes: red: O; gray: C; white: H.

cyclohexanone adsorption with increasing temperature. Collectively, these results provide evidence that the polarity of the zeolite pore alters the structure of intraporous H-bonding alcohol networks, which influence adsorption and activation free energies of MPVO reactions catalyzed by Sn-Beta zeolites.

**3.4. Adsorption and Activation Enthalpies and Entropies Measured in the Presence of Different Intraporous Solvent Structures.** Apparent MPVO rate constants ( $k_{\text{app}}$ ) and cyclohexanone adsorption equilibrium constants ( $K_{\text{ads}}$ ) can be expressed in terms of enthalpic and entropic contributions that comprise free energy differences between final and initial states:

$$k_{\text{app}} = \frac{k_{\text{b}}T}{h} e^{-\Delta G_{\text{app}}/RT} = \frac{k_{\text{b}}T}{h} e^{-\Delta H_{\text{app}}/RT} e^{\Delta S_{\text{app}}/R} \quad (8)$$

$$K_{\text{ads}} = e^{-\Delta G_{\text{ads}}/RT} = e^{-\Delta H_{\text{ads}}/RT} e^{\Delta S_{\text{ads}}/R} \quad (9)$$

where  $k_{\text{b}}$  is Boltzmann's constant,  $T$  is the reaction temperature,  $h$  is Planck's constant, and  $R$  is the ideal gas constant.  $\Delta H_{\text{ads}}$  and  $\Delta S_{\text{ads}}$  are the enthalpy and entropy, respectively, of cyclohexanone adsorption and reflect differences between the final adsorbed 2-butanol–cyclohexanone adduct and 2-butanol in solution and the 2-butanol-covered open Sn site and cyclohexanone in solution.  $\Delta H_{\text{app}}$  and  $\Delta S_{\text{app}}$  are the apparent enthalpy and entropy, respectively, of activation and reflect differences between the hydride-shift transition state and the coadsorbed 2-butanol–cyclohexanone adduct. Values of  $\Delta H_{\text{ads}}$ ,  $\Delta S_{\text{ads}}$ ,  $\Delta H_{\text{app}}$ , and  $\Delta S_{\text{app}}$  extracted from traditional Arrhenius plots (data shown in Figure 2) were found to be strongly intercorrelated due to confounding statistical linear enthalpy–entropy compensation that arises from uncertainty in experimental data and may not reflect purely chemical thermodynamic trends (details in section S11 of the Supporting Information).<sup>106–108</sup> Here, values of  $\Delta H$  and  $\Delta G$  are determined by transforming the typical  $1/T$  axis of an Arrhenius-type plot (i.e.,  $\ln(k)$  vs  $1/T$ ) to be relative to the harmonic mean temperature ( $T_{\text{hm}}$ ) of the system (i.e.,  $\ln(k)$  vs  $[1/T - 1/T_{\text{hm}}]$ ), such that the vertical axis bisects the data set. This attenuates compensating errors associated with the nonlinear regression of  $\Delta H$  and  $\Delta S$  and traditional Arrhenius analyses that arise from extrapolation of small uncertainties in measured activation (or adsorption) slopes (e.g., enthalpies) to a vertical axis (defined at  $1/T = 0$ ) far from the measured experimental temperature range that can result in large changes in  $\Delta S$  leading to statistically coupled values of  $\Delta H$  and  $\Delta S$  (details in section S11 of the Supporting Information).<sup>106–108</sup>

Values of  $\Delta H_{\text{ads}}$ ,  $\Delta S_{\text{ads}}$ ,  $\Delta H_{\text{app}}$ , and  $\Delta S_{\text{app}}$  determined from this analysis on Sn-Beta-F(302) and Sn-Beta-OH(326) in a 2-butanol solvent are listed in Table 2. The modest enthalpic

**Table 2. Values of  $\Delta H_{\text{ads}}$ ,  $\Delta S_{\text{ads}}$ ,  $\Delta H_{\text{app}}$ , and  $\Delta S_{\text{app}}$  Determined from Experimental Kinetics Measured on Sn-Beta-F(302) and Sn-Beta-OH(326) in a 2-Butanol Solvent**

zeolite	$\Delta H_{\text{ads}}^a$	$\Delta S_{\text{ads}}^b$	$\Delta H_{\text{app}}^a$	$\Delta S_{\text{app}}^b$
Sn-Beta-F(302)	$43 \pm 10$	$134 \pm 24$	$33 \pm 8$	$-149 \pm 19$
Sn-Beta-OH(326)	$14 \pm 5$	$64 \pm 13$	$40 \pm 3$	$-148 \pm 9$
$\Delta\Delta(\text{F-OH})$	29	70	-7	-1

<sup>a</sup>Units of  $\Delta H$  are  $\text{kJ mol}^{-1}$ . <sup>b</sup>Units of  $\Delta S$  are  $\text{J mol}^{-1} \text{K}^{-1}$ .

barrier on Sn-Beta-F(302) and Sn-Beta-OH(326) ( $\Delta H_{\text{app}} = 33$  and  $40 \text{ kJ mol}^{-1}$ , respectively) for the formation of the hydride shift transition state from the coadsorbed 2-butanol–cyclohexanone adduct reflects the deprotonation of 2-butanol to form the adsorbed alkoxide and water and the partial cleavage of the  $\alpha\text{C-H}$  bond of 2-butanol required to form the six-membered ring transition state.<sup>79</sup> The change in the apparent activation entropy measured on both Sn-Beta catalysts ( $\Delta S_{\text{app}} = -148$  to  $-149 \text{ J mol}^{-1} \text{K}^{-1}$ ) reflects the change in entropy between the hydride shift transition state and the coadsorbed 2-butanol–cyclohexanone adduct. This decrease in entropy upon transition state formation is likely caused by the loss of frustrated rotational and quasi-translational degrees of freedom present in noncovalently adsorbed species confined within zeolite catalysts.<sup>50,109</sup> The apparent enthalpic activation barrier

( $\Delta H_{\text{app}}$ ) is about 7 kJ mol<sup>-1</sup> smaller on Sn-Beta-F than Sn-Beta-OH (Table 2), while both catalysts exhibit a similar entropy of activation ( $\sim -148$  J mol<sup>-1</sup> K<sup>-1</sup>). These differences in activation parameters reflect apparent activation free energy barriers that are  $\sim 7$  kJ mol<sup>-1</sup> (evaluated at 373 K) lower on Sn-Beta-F than on Sn-Beta-OH, which give rise to zero-order rate constants that are  $\sim 10\times$  larger on Sn-Beta-F(302) than on Sn-Beta-OH(326) (Figure 3). The lower apparent activation barriers on Sn-Beta-F(302) are likely due to the preferential enthalpic stabilization of the hydride-shift transition state, relative to the coadsorbed 2-butanol–cyclohexanone adduct, by the more tightly ordered intraporous solvent structure present in Sn-Beta-F (Figure 5) as the MPVO reaction is catalyzed by open Sn sites confined within pores of the same size in both Sn-Beta zeolites.

Adsorption of cyclohexanone within Sn-Beta-F(302) and Sn-Beta-OH(326) from the 2-butanol solution phase results in positive values of  $\Delta H_{\text{ads}}$  (43 and 14 kJ mol<sup>-1</sup>, respectively) and  $\Delta S_{\text{ads}}$  (134 and 64 J mol<sup>-1</sup> K<sup>-1</sup>, respectively) despite confinement and adsorption of cyclohexanone at the open Sn site within the Beta framework from the solution phase. Thus, occlusion and coordination of cyclohexanone at an open Sn site result in an enthalpic penalty, but a net gain in entropy, relative to the initial state, upon adsorption. This behavior contrasts classical adsorption within microporous materials from the gas phase, which is typically characterized by negative adsorption enthalpies and entropies due to favorable dispersive interactions between the adsorbate and the zeolite pore walls and coordination at the adsorption site.<sup>110–113</sup> The gain in entropy upon adsorption observed here is likely not due to loss of a solution phase solvation shell or displacement of adsorbed 2-butanol from the open Sn site as the change in entropy would be expected to be similar on both Sn-Beta-F(302) and Sn-Beta-OH(326), which contain similar active sites in the same 2-butanol solution phase. IR spectra (Figure 5) indicate that 2-butanol adsorbed within hydrophobic Sn-Beta-F form ordered H-bonding networks that deviate in structure from 2-butanol in the bulk or that confined within hydrophilic Sn-Beta-OH. Additionally, adsorption within a tightly ordered solvent, as are often found within hydrophobic pockets of enzymatic active sites, is dominated by the breakup of solvent–solvent interactions and an increase in solvent disorder leading to higher solvent reorganization enthalpies, which may be partially compensated by an increase in solvent reorganization entropy.<sup>114,115</sup> Together, these spectroscopic and kinetic data suggest that adsorption of cyclohexanone within Sn-Beta-F(302) disrupts the ordered solvent structure confined within hydrophobic pores and incurs an enthalpic penalty, but results in the liberation of tightly ordered 2-butanol molecules, giving rise to an increase in entropy relative to the initial state of solution phase cyclohexanone.

In contrast to the less positive apparent activation enthalpy and similar apparent activation entropy on Sn-Beta-F, both the enthalpy and entropy of cyclohexanone adsorption from a 2-butanol solvent are significantly more positive on Sn-Beta-F(302) than on Sn-Beta-OH(326) ( $\Delta\Delta(\text{F–OH})$ : 29 kJ mol<sup>-1</sup> and 70 J mol<sup>-1</sup> K<sup>-1</sup>, respectively; Table 2). This indicates that confinement and adsorption of cyclohexanone within the 2-butanol filled pores of Sn-Beta-OH are more enthalpically favorable than in Sn-Beta-F but result in a smaller gain in entropy. This difference in cyclohexanone adsorption entropy gives rise to the large deviation observed in cyclohexanone adsorption equilibrium constants (Figure 3) between Sn-Beta-

F(302) and Sn-Beta-OH(326) with increasing temperature because the entropy of adsorption becomes a more dominant contributor to the free energy of adsorption at elevated temperatures. As a result, the free energy of adsorption within hydrophobic Sn-Beta-F becomes more negative with increasing temperature, which gives rise to cyclohexanone coverages that increase with temperature (Figure 4). This behavior causes the dramatic shift in the onset of the zero-order kinetic regime to nearly a  $10\times$  lower value of cyclohexanone activity with increasing temperature (Figure 2). Moreover, these data highlight the importance of extracting adsorption and activation enthalpies and entropies from rate and equilibrium constants measured as a function of both thermodynamic activity (or concentration) and temperature instead of solely from single point rate measurements, which are often assumed to remain within a given kinetic regime with changing reaction temperature. Doing so becomes increasingly important when H-bonding solvents become confined within the subnanometer pores of zeolite catalysts because the transition between different kinetic regimes can vary strongly with temperature due to the complex interactions between adsorbates and the catalyst surface.

#### 4. CONCLUSION

While the polarity of the zeolite pore that confines Lewis acidic active sites has been recognized to influence catalytic turnover rates in aqueous media, the results presented here describe how catalytic and adsorption phenomena in nonaqueous H-bonding solvents are influenced by the polarity of the secondary solvating environment. Sn-Beta zeolites synthesized via direct hydrothermal crystallization in the presence of F<sup>-</sup> anions (Sn-Beta-F) and from postsynthetic grafting of anhydrous SnCl<sub>4</sub> precursors at defect sites in dealuminated Beta zeolites (Sn-Beta-OH) contain similar fractions of their framework Sn atoms as Lewis acid sites, but Sn-Beta-OH zeolites contain  $>10\times$  more hydrophilic SiOH groups, as determined from IR spectra measured after titration of surface sites by CD<sub>3</sub>CN. Initial turnover rates (333–393 K; normalized per open Sn site counted by CD<sub>3</sub>CN) of the MPVO transfer hydrogenation reaction between 2-butanol and cyclohexanone measured in a 2-butanol solvent increase linearly on both Sn-Beta-F and Sn-Beta-OH zeolites at low cyclohexanone activities ( $a_c < 0.02$ ) and approach a zero-order regime with increasing cyclohexanone activity ( $a_c > 0.1$ ), reflecting a change in the MARI from a 2-butanol-covered open Sn site to a coadsorbed 2-butanol–cyclohexanone adduct. At low reaction temperatures ( $<353$  K), first-order initial MPVO turnover rates (per open Sn) are similar (within  $2\times$ ) on Sn-Beta-F and Sn-Beta-OH but become nearly  $10\times$  larger on Sn-Beta-F in the zero-order kinetic regime (333–393 K) and in the first-order regime at elevated temperatures ( $>353$  K). Apparent zero-order rate constants (per open Sn) are  $\sim 10\times$  larger on Sn-Beta-F than on Sn-Beta-OH at all temperatures (333–393 K), reflecting the preferential stabilization of the hydride-shift transition state within hydrophobic Sn-Beta-F zeolites. Cyclohexanone adsorption equilibrium constants, extracted from kinetic data, increase with increasing temperature on both Sn-Beta zeolites but are more sensitive to changes in temperature on Sn-Beta-F ( $\sim 10\times$  larger at 393 K than 333 K) than on Sn-Beta-OH ( $\sim 2.5\times$  larger at 393 K than 333 K), suggesting that the intraporous 2-butanol solvent environment in Sn-Beta-OH changes more

similarly to the bulk solution than that confined in hydrophobic Sn-Beta-F.

IR spectra of 2-butanol adsorbed at different coverages in Sn-Beta zeolites reveal the preferential stabilization of dimeric 2-butanol networks in hydrophobic Sn-Beta-F zeolites near pore filling, whereas the structure of 2-butanol adsorbed within hydrophilic Sn-Beta-OH more closely resembles that of the bulk liquid solvent. The hydrophobic pores of Sn-Beta-F appear to inhibit the formation of extended liquidlike 2-butanol oligomers and instead give rise to ordered H-bonded 2-butanol networks, a phenomenon similar to that observed for water confined within microporous hydrophobic voids. These ordered solvent structures are reminiscent of those observed in biological catalysts, which give rise to entropically favored adsorption and transition state formation due to the reorganization and displacement of H-bonded solvent molecules. The different intraporous 2-butanol solvent environments observed in hydrophobic and hydrophilic Sn-Beta zeolites manifests in the activation and adsorption enthalpies and entropies that comprise the free energy landscape of MPVO catalysis. The more tightly ordered 2-butanol solvent structure present in the pores of Sn-Beta-F leads to lower apparent activation enthalpies than those observed for Sn-Beta-OH, which reflect smaller apparent free energy barriers (by  $\sim 7$  kJ mol<sup>-1</sup> at 373 K) for the formation of the hydride-shift transition state from the coadsorbed 2-butanol–cyclohexanone adduct on hydrophobic Sn-Beta-F zeolites. Cyclohexanone adsorption enthalpies and entropies on both Sn-Beta-F and Sn-Beta-OH are both positive, indicating that adsorption and confinement of cyclohexanone within Sn-Beta give rise to an enthalpic penalty, but a net gain in entropy, relative to the initial state. Furthermore, the adsorption of cyclohexanone within the 2-butanol-filled pores of hydrophilic Sn-Beta-OH is more enthalpically favorable than in Sn-Beta-F ( $\Delta\Delta H_{\text{ads}}(\text{F-OH})$ : 29 kJ mol<sup>-1</sup>) but results in a smaller gain in entropy ( $\Delta\Delta S_{\text{ads}}(\text{F-OH})$ : 70 J mol<sup>-1</sup> K<sup>-1</sup>), likely because adsorption within an ordered H-bonding network is dominated by the breakup of solvent–solvent interactions that result in an increase in solvent disorder. The disruption of such ordered solvent structures present within hydrophobic Sn-Beta-F catalysts results in more positive enthalpies of adsorption, which are partially compensated by an increase in the solvent reorganization entropy. Collectively, these results emphasize how hydrophobic zeolite pores order intraporous H-bonding networks, similar to how biological catalysts use hydrophobic amino acid residues to regulate solvent structure within active site pockets, and highlight the importance of the zeolite framework polarity on catalysis within microporous voids. Moreover, the ability of the zeolite pore to control the structure of confined nonaqueous H-bonding solvent networks offers a unique dimension for the design and engineering of microporous adsorbents and catalysts beyond the active site.

## ■ ASSOCIATED CONTENT

### Supporting Information

The Supporting Information is available free of charge at <https://pubs.acs.org/doi/10.1021/jacs.0c09825>.

XRD patterns, N<sub>2</sub> adsorption isotherms, UV–vis spectra, IR spectra of adsorbed CD<sub>3</sub>CN and 2-butanol, deconvolution of CD<sub>3</sub>CN IR spectra, control and anhydrous MPVO rates, derivation of MPVO rate

equations, statistical analysis of enthalpies and entropies (PDF)

## ■ AUTHOR INFORMATION

### Corresponding Author

**Yuriy Román-Leshkov** – Department of Chemical Engineering, Massachusetts Institute of Technology, Cambridge, Massachusetts 02139, United States; [orcid.org/0000-0002-0025-4233](https://orcid.org/0000-0002-0025-4233); Email: [yroman@mit.edu](mailto:yroman@mit.edu)

### Authors

**John R. Di Iorio** – Department of Chemical Engineering, Massachusetts Institute of Technology, Cambridge, Massachusetts 02139, United States

**Blake A. Johnson** – Department of Chemical Engineering, Massachusetts Institute of Technology, Cambridge, Massachusetts 02139, United States

Complete contact information is available at: <https://pubs.acs.org/10.1021/jacs.0c09825>

### Notes

The authors declare no competing financial interest.

## ■ ACKNOWLEDGMENTS

J.R.D., B.A.J., and Y.R.-L. thank the U.S. Department of Energy, Office of Basic Energy Sciences under Award DE-SC0016214 for support. We also thank Dr. Jennifer Lewis for the preparation of the Sn-Beta-F zeolites and Alexander Khechfe and Thejas Wesley for helpful discussions and manuscript review.

## ■ REFERENCES

- (1) Abel, R.; Young, T.; Farid, R.; Berne, B. J.; Friesner, R. A. Role of the Active-Site Solvent in the Thermodynamics of Factor Xa Ligand Binding. *J. Am. Chem. Soc.* **2008**, *130*, 2817–2831.
- (2) Grunwald, E.; Steel, C. Solvent Reorganization and Thermodynamic Enthalpy-Entropy Compensation. *J. Am. Chem. Soc.* **1995**, *117*, 5687–5692.
- (3) Breiten, B.; Lockett, M. R.; Sherman, W.; Fujita, S.; Al-Sayah, M.; Lange, H.; Bowers, C. M.; Heroux, A.; Krilov, G.; Whitesides, G. M. Water Networks Contribute to Enthalpy/Entropy Compensation in Protein–Ligand Binding. *J. Am. Chem. Soc.* **2013**, *135*, 15579–15584.
- (4) Snyder, P. W.; Lockett, M. R.; Moustakas, D. T.; Whitesides, G. M. Is It the Shape of the Cavity, or the Shape of the Water in the Cavity? *Eur. Phys. J.: Spec. Top.* **2014**, *223*, 853–891.
- (5) Lemieux, R. U. How Water Provides the Impetus for Molecular Recognition in Aqueous Solution. *Acc. Chem. Res.* **1996**, *29*, 373–380.
- (6) Degnan, T. F. The Implications of the Fundamentals of Shape Selectivity for the Development of Catalysts for the Petroleum and Petrochemical Industries. *J. Catal.* **2003**, *216*, 32–46.
- (7) Gallego, E. M.; Portilla, M. T.; Paris, C.; León-Escamilla, A.; Boronat, M.; Moliner, M.; Corma, A. Ab Initio Synthesis of Zeolites for Preestablished Catalytic Reactions. *Science* **2017**, *355*, 1051.
- (8) Barthomeuf, D. A General Hypothesis on Zeolites Physicochemical Properties. Applications to Adsorption, Acidity, Catalysis, and Electrochemistry. *J. Phys. Chem.* **1979**, *83*, 249–256.
- (9) Noh, G.; Shi, Z.; Zones, S. I.; Iglesia, E. Isomerization and B-Scission Reactions of Alkanes on Bifunctional Metal-Acid Catalysts: Consequences of Confinement and Diffusional Constraints on Reactivity and Selectivity. *J. Catal.* **2018**, *368*, 389–410.
- (10) Janda, A.; Vlasisavljevic, B.; Lin, L.-C.; Smit, B.; Bell, A. T. Effects of Zeolite Structural Confinement on Adsorption Thermodynamics and Reaction Kinetics for Monomolecular Cracking and

Dehydrogenation of N-Butane. *J. Am. Chem. Soc.* **2016**, *138*, 4739–4756.

(11) Jones, A. J.; Zones, S. I.; Iglesia, E. Implications of Transition State Confinement within Small Voids for Acid Catalysis. *J. Phys. Chem. C* **2014**, *118*, 17787–17800.

(12) Derouane, E. G. Zeolites as Solid Solvents. *J. Mol. Catal. A: Chem.* **1998**, *134*, 29–45.

(13) Gounder, R.; Iglesia, E. The Catalytic Diversity of Zeolites: Confinement and Solvation Effects within Voids of Molecular Dimensions. *Chem. Commun.* **2013**, *49*, 3491–3509.

(14) Vega-Vila, J. C.; Harris, J. W.; Gounder, R. Controlled Insertion of Tin Atoms into Zeolite Framework Vacancies and Consequences for Glucose Isomerization Catalysis. *J. Catal.* **2016**, *344*, 108–120.

(15) Van Der Graaff, W. N. P.; Li, G.; Mezari, B.; Pidko, E. A.; Hensen, E. J. M. Synthesis of Sn-Beta with Exclusive and High Framework Sn Content. *ChemCatChem* **2015**, *7*, 1152–1160.

(16) Dijkmans, J.; Demol, J.; Houthoofd, K.; Huang, S.; Pontikes, Y.; Sels, B. Post-Synthesis Sn $\beta$ : An Exploration of Synthesis Parameters and Catalysis. *J. Catal.* **2015**, *330*, 545–557.

(17) Gounder, R.; Davis, M. E. Beyond Shape Selective Catalysis with Zeolites: Hydrophobic Void Spaces in Zeolites Enable Catalysis in Liquid Water. *AIChE J.* **2013**, *59*, 3349–3358.

(18) Corma, A.; Nemeth, L. T.; Renz, M.; Valencia, S. Sn-Zeolite Beta as a Heterogeneous Chemoselective Catalyst for Baeyer–Villiger Oxidations. *Nature* **2001**, *412*, 423–425.

(19) Moliner, M. State of the Art of Lewis Acid-Containing Zeolites: Lessons from Fine Chemistry to New Biomass Transformation Processes. *Dalton Trans.* **2014**, *43*, 4197–4208.

(20) Román-Leshkov, Y.; Davis, M. E. Activation of Carbonyl-Containing Molecules with Solid Lewis Acids in Aqueous Media. *ACS Catal.* **2011**, *1*, 1566–1580.

(21) Luo, H. Y.; Lewis, J. D.; Román-Leshkov, Y. Lewis Acid Zeolites for Biomass Conversion: Perspectives and Challenges on Reactivity, Synthesis, and Stability. *Annu. Rev. Chem. Biomol. Eng.* **2016**, *7*, 663–692.

(22) Corma, A.; Domine, M. E.; Nemeth, L.; Valencia, S. Al-Free Sn-Beta Zeolite as a Catalyst for the Selective Reduction of Carbonyl Compounds (Meerwein-Ponndorf-Verley Reaction). *J. Am. Chem. Soc.* **2002**, *124*, 3194–3195.

(23) Shantz, D. F.; Schmedt Auf Der Günne, J.; Koller, H.; Lobo, R. F. Multiple-Quantum 1H MAS NMR Studies of Defect Sites in As-Made All-Silica ZSM-12 Zeolite. *J. Am. Chem. Soc.* **2000**, *122*, 6659–6663.

(24) Koller, H.; Lobo, R. F.; Burkett, S. L.; Davis, M. E. SiO–HOSi Hydrogen Bonds in As-Synthesized High-Silica Zeolites. *J. Phys. Chem.* **1995**, *99*, 12588–12596.

(25) Cambor, M. A.; Villacusa, L. A.; Díaz-Cabañas, M. J. Synthesis of All-Silica and High-Silica Molecular Sieves in Fluoride Media. *Top. Catal.* **1999**, *9*, 59–76.

(26) Rasaiah, J. C.; Garde, S.; Hummer, G. Water in Nonpolar Confinement: From Nanotubes to Proteins and Beyond. *Annu. Rev. Phys. Chem.* **2008**, *59*, 713–740.

(27) Cailliez, F.; Stirnemann, G.; Boutin, A.; Demachy, I.; Fuchs, A. H. Does Water Condense in Hydrophobic Cavities? A Molecular Simulation Study of Hydration in Heterogeneous Nanopores. *J. Phys. Chem. C* **2008**, *112*, 10435–10445.

(28) Bukowski, B. C.; Bates, J. S.; Gounder, R.; Greeley, J. Defect-Mediated Ordering of Condensed Water Structures in Microporous Zeolites. *Angew. Chem., Int. Ed.* **2019**, *58*, 16422–16426.

(29) Agrawal, K. V.; Shimizu, S.; Drahushuk, L. W.; Kilcoyne, D.; Strano, M. S. Observation of Extreme Phase Transition Temperatures of Water Confined inside Isolated Carbon Nanotubes. *Nat. Nanotechnol.* **2017**, *12*, 267–273.

(30) Chandler, D. Interfaces and the Driving Force of Hydrophobic Assembly. *Nature* **2005**, *437*, 640–647.

(31) Zhang, C.; Gygi, F.; Galli, G. Strongly Anisotropic Dielectric Relaxation of Water at the Nanoscale. *J. Phys. Chem. Lett.* **2013**, *4*, 2477–2481.

(32) Fumagalli, L.; Esfandiari, A.; Fabregas, R.; Hu, S.; Ares, P.; Janardanan, A.; Yang, Q.; Radha, B.; Taniguchi, T.; Watanabe, K.; Gomila, G.; Novoselov, K. S.; Geim, A. K. Anomalous Low Dielectric Constant of Confined Water. *Science* **2018**, *360*, 1339.

(33) Mondal, S.; Bagchi, B. Water in Carbon Nanotubes: Pronounced Anisotropy in Dielectric Dispersion and Its Microscopic Origin. *J. Phys. Chem. Lett.* **2019**, *10*, 6287–6292.

(34) Mallon, E. E.; Babineau, I. J.; Kranz, J. I.; Guefrachi, Y.; Siepmann, J. I.; Bhan, A.; Tsapatsis, M. Correlations for Adsorption of Oxygenates onto Zeolites from Aqueous Solutions. *J. Phys. Chem. B* **2011**, *115*, 11431–11438.

(35) Stelzer, J.; Paulus, M.; Hunger, M.; Weitkamp, J. Hydrophobic Properties of All-Silica Zeolite Beta. *Microporous Mesoporous Mater.* **1998**, *22*, 1–8.

(36) Langhendries, G.; De Vos, D. E.; Baron, G. V.; Jacobs, P. A. Quantitative Sorption Experiments on Ti-Zeolites and Relation with  $\alpha$ -Olefin Oxidation by H<sub>2</sub>O<sub>2</sub>. *J. Catal.* **1999**, *187*, 453–463.

(37) Parton, R. F.; Neys, P. E.; Jacobs, P. A.; Sosa, R. C.; Rouxhet, P. G. Iron–Phthalocyanine Immobilized on Activated Carbon Black: A Selective Catalyst for Alkane Oxidation. *J. Catal.* **1996**, *164*, 341–346.

(38) Parton, R. F.; Peere, G. J.; Neys, P. E.; Jacobs, P. A.; Claessens, R.; Baron, G. V. Cyclohexane Oxidation with Tertiary-Butylhydroperoxide Catalyzed by Iron-Phthalocyanines Homogeneously and Occluded in Y Zeolite. *J. Mol. Catal. A: Chem.* **1996**, *113*, 445–454.

(39) Chen, N. Y. Hydrophobic Properties of Zeolites. *J. Phys. Chem.* **1976**, *80*, 60–64.

(40) Flanigen, E. M.; Bennett, J. M.; Grose, R. W.; Cohen, J. P.; Patton, R. L.; Kirchner, R. M.; Smith, J. V. Silicalite, a New Hydrophobic Crystalline Silica Molecular Sieve. *Nature* **1978**, *271*, 512–516.

(41) Van Den Bergh, M.; Krajnc, A.; Voorspoels, S.; Tavares, S. R.; Mullens, S.; Beurrois, I.; Maurin, G.; Mali, G.; De Vos, D. E. Highly Selective Removal of Perfluorinated Contaminants by Adsorption on All-Silica Zeolite Beta. *Angew. Chem., Int. Ed.* **2020**, *59*, 14086–14090.

(42) Li, G.; Wang, B.; Resasco, D. E. Water-Mediated Heterogeneously Catalyzed Reactions. *ACS Catal.* **2020**, *10*, 1294–1309.

(43) Harris, J. W.; Bates, J. S.; Bukowski, B. C.; Greeley, J.; Gounder, R. Opportunities in Catalysis over Metal-Zeotypes Enabled by Descriptions of Active Centers Beyond Their Binding Site. *ACS Catal.* **2020**, *10*, 9476–9495.

(44) Gould, N. S.; Xu, B. Temperature-Programmed Desorption of Pyridine on Zeolites in the Presence of Liquid Solvents. *ACS Catal.* **2018**, *8*, 8699–8708.

(45) Gould, N. S.; Li, S.; Cho, H. J.; Landfield, H.; Caratzoulas, S.; Vlachos, D.; Bai, P.; Xu, B. Understanding Solvent Effects on Adsorption and Protonation in Porous Catalysts. *Nat. Commun.* **2020**, *11*, 1060.

(46) Bai, P.; Siepmann, J. I.; Deem, M. W. Adsorption of Glucose into Zeolite Beta from Aqueous Solution. *AIChE J.* **2013**, *59*, 3523–3529.

(47) Cordon, M. J.; Harris, J. W.; Vega-Vila, J. C.; Bates, J. S.; Kaur, S.; Gupta, M.; Witzke, M. E.; Wegener, E. C.; Miller, J. T.; Flaherty, D. W.; Hibbitts, D. D.; Gounder, R. Dominant Role of Entropy in Stabilizing Sugar Isomerization Transition States within Hydrophobic Zeolite Pores. *J. Am. Chem. Soc.* **2018**, *140*, 14244–14266.

(48) Eckstein, S.; Hintermeier, P. H.; Olarte, M. V.; Liu, Y.; Baráth, E.; Lercher, J. A. Elementary Steps and Reaction Pathways in the Aqueous Phase Alkylation of Phenol with Ethanol. *J. Catal.* **2017**, *352*, 329–336.

(49) Bates, J. S.; Bukowski, B.; Greeley, J. P.; Gounder, R. Structure and Solvation of Confined Water and Water-Ethanol Clusters within Microporous Brønsted Acids and Their Effects on Ethanol Dehydration Catalysis. *Chem. Sci.* **2020**, *11*, 7102–7122.

(50) Bukowski, B. C.; Bates, J. S.; Gounder, R.; Greeley, J. First Principles, Microkinetic, and Experimental Analysis of Lewis Acid Site Speciation During Ethanol Dehydration on Sn-Beta Zeolites. *J. Catal.* **2018**, *365*, 261–276.

- (51) Bates, J. S.; Gounder, R. Influence of Confining Environment Polarity on Ethanol Dehydration Catalysis by Lewis Acid Zeolites. *J. Catal.* **2018**, *365*, 213–226.
- (52) Harris, J. W.; Cordon, M. J.; Di Iorio, J. R.; Vega-Vila, J. C.; Ribeiro, F. H.; Gounder, R. Titration and Quantification of Open and Closed Lewis Acid Sites in Sn-Beta Zeolites That Catalyze Glucose Isomerization. *J. Catal.* **2016**, *335*, 141–154.
- (53) Gounder, R.; Davis, M. E. Monosaccharide and Disaccharide Isomerization over Lewis Acid Sites in Hydrophobic and Hydrophilic Molecular Sieves. *J. Catal.* **2013**, *308*, 176–188.
- (54) Bregante, D. T.; Johnson, A. M.; Patel, A. Y.; Ayla, E. Z.; Cordon, M. J.; Bukowski, B. C.; Greeley, J.; Gounder, R.; Flaherty, D. W. Cooperative Effects between Hydrophilic Pores and Solvents: Catalytic Consequences of Hydrogen Bonding on Alkene Epoxidation in Zeolites. *J. Am. Chem. Soc.* **2019**, *141*, 7302–7319.
- (55) Wang, L.; Sun, J.; Meng, X.; Zhang, W.; Zhang, J.; Pan, S.; Shen, Z.; Xiao, F.-S. A Significant Enhancement of Catalytic Activities in Oxidation with H<sub>2</sub>O<sub>2</sub> over the TS-1 Zeolite by Adjusting the Catalyst Wettability. *Chem. Commun.* **2014**, *50*, 2012–2014.
- (56) Wu, L.; Tang, Z.; Yu, Y.; Yao, X.; Liu, W.; Li, L.; Yan, B.; Liu, Y.; He, M. Facile Synthesis of a High-Performance Titanosilicate Catalyst with Controllable Defective Ti(OSi)<sub>3</sub>OH Sites. *Chem. Commun.* **2018**, *54*, 6384–6387.
- (57) Bregante, D. T.; Flaherty, D. W. Impact of Specific Interactions among Reactive Surface Intermediates and Confined Water on Epoxidation Catalysis and Adsorption in Lewis Acid Zeolites. *ACS Catal.* **2019**, *9*, 10951–10962.
- (58) Luo, H. Y.; Consoli, D. F.; Gunther, W. R.; Román-Leshkov, Y. Investigation of the Reaction Kinetics of Isolated Lewis Acid Sites in Beta Zeolites for the Meerwein–Ponndorf–Verley Reduction of Methyl Levulinate to  $\Gamma$ -Valerolactone. *J. Catal.* **2014**, *320*, 198–207.
- (59) Wang, J.; Okumura, K.; Jaenicke, S.; Chuah, G.-K. Post-Synthesized Zirconium-Containing Beta Zeolite in Meerwein–Ponndorf–Verley Reduction: Pros and Cons. *Appl. Catal., A* **2015**, *493*, 112–120.
- (60) Van Grieken, R.; Martos, C.; Sánchez-Sánchez, M.; Serrano, D. P.; Melero, J. A.; Iglesias, J.; Cubero, A. G. Synthesis of Sn–Silicalite from Hydrothermal Conversion of SiO<sub>2</sub>–SnO<sub>2</sub> Xerogels. *Microporous Mesoporous Mater.* **2009**, *119*, 176–185.
- (61) Thommes, M.; Cychosz, K. A. Physical Adsorption Characterization of Nanoporous Materials: Progress and Challenges. *Adsorption* **2014**, *20*, 233–250.
- (62) Bermejo-Deval, R.; Orazov, M.; Gounder, R.; Hwang, S.-J.; Davis, M. E. Active Sites in Sn-Beta for Glucose Isomerization to Fructose and Epimerization to Mannose. *ACS Catal.* **2014**, *4*, 2288–2297.
- (63) Boronat, M.; Concepción, P.; Corma, A.; Renz, M.; Valencia, S. Determination of the Catalytically Active Oxidation Lewis Acid Sites in Sn-Beta Zeolites, and Their Optimisation by the Combination of Theoretical and Experimental Studies. *J. Catal.* **2005**, *234*, 111–118.
- (64) Schwartz, T. J.; Wesley, T. S.; Dumesic, J. A. Modifying the Surface Properties of Heterogeneous Catalysts Using Polymer-Derived Microenvironments. *Top. Catal.* **2016**, *59*, 19–28.
- (65) Wolf, P.; Valla, M.; Núñez-Zarur, F.; Comas-Vives, A.; Rossini, A. J.; Firth, C.; Kallas, H.; Lesage, A.; Emsley, L.; Copéret, C.; Hermans, I. Correlating Synthetic Methods, Morphology, Atomic-Level Structure, and Catalytic Activity of Sn-B Zeolites. *ACS Catal.* **2016**, *6*, 4047–4063.
- (66) Rai, N.; Caratzoulas, S.; Vlachos, D. G. Role of Silanol Group in Sn-Beta Zeolite for Glucose Isomerization and Epimerization Reactions. *ACS Catal.* **2013**, *3*, 2294–2298.
- (67) Bermejo-Deval, R.; Assary, R. S.; Nikolla, E.; Moliner, M.; Román-Leshkov, Y.; Hwang, S.-J.; Palsdotir, A.; Silverman, D.; Lobo, R. F.; Curtiss, L. A.; Davis, M. E. Metalloenzyme-Like Catalyzed Isomerizations of Sugars by Lewis Acid Zeolites. *Proc. Natl. Acad. Sci. U. S. A.* **2012**, *109*, 9727.
- (68) Bare, S. R.; Kelly, S. D.; Sinkler, W.; Low, J. J.; Modica, F. S.; Valencia, S.; Corma, A.; Nemeth, L. T. Uniform Catalytic Site in Sn-B-Zeolite Determined Using X-Ray Absorption Fine Structure. *J. Am. Chem. Soc.* **2005**, *127*, 12924–12932.
- (69) Wolf, P.; Liao, W.-C.; Ong, T.-C.; Valla, M.; Harris, J. W.; Gounder, R.; Van Der Graaff, W. N. P.; Pidko, E. A.; Hensen, E. J. M.; Ferrini, P.; Dijkmans, J.; Sels, B.; Hermans, I.; Copéret, C. Identifying Sn Site Heterogeneities Prevalent among Sn-Beta Zeolites. *Helv. Chim. Acta* **2016**, *99*, 916–927.
- (70) Boronat, M.; Corma, A.; Renz, M.; Viruela, P. M. Predicting the Activity of Single Isolated Lewis Acid Sites in Solid Catalysts. *Chem. - Eur. J.* **2006**, *12*, 7067–7077.
- (71) Madon, R. J.; Boudart, M. Experimental Criterion for the Absence of Artifacts in the Measurement of Rates of Heterogeneous Catalytic Reactions. *Ind. Eng. Chem. Fundam.* **1982**, *21*, 438–447.
- (72) Wittig, R.; Lohmann, J.; Gmehling, J. Vapor-Liquid Equilibria by UNIFAC Group Contribution. 6. Revision and Extension. *Ind. Eng. Chem. Res.* **2003**, *42*, 183–188.
- (73) Hansen, H. K.; Rasmussen, P.; Fredenslund, A.; Schiller, M.; Gmehling, J. Vapor-Liquid Equilibria by UNIFAC Group Contribution. 5. Revision and Extension. *Ind. Eng. Chem. Res.* **1991**, *30*, 2352–2355.
- (74) Fredenslund, A.; Jones, R. L.; Prausnitz, J. M. Group-Contribution Estimation of Activity Coefficients in Nonideal Liquid Mixtures. *AIChE J.* **1975**, *21*, 1086–1099.
- (75) Van Der Waal, J. C.; Tan, K.; Van Bekkum, H. Zeolite Titanium Beta: A Selective and Water Resistant Catalyst in Meerwein–Ponndorf–Verley–Oppenauer Reactions. *Catal. Lett.* **1996**, *41*, 63–67.
- (76) Assary, R. S.; Curtiss, L. A.; Dumesic, J. A. Exploring Meerwein–Ponndorf–Verley Reduction Chemistry for Biomass Catalysis Using a First-Principles Approach. *ACS Catal.* **2013**, *3*, 2694–2704.
- (77) Cohen, R.; Graves, C. R.; Nguyen, S. T.; Martin, J. M. L.; Ratner, M. A. The Mechanism of Aluminum-Catalyzed Meerwein–Schmidt–Ponndorf–Verley Reduction of Carbonyls to Alcohols. *J. Am. Chem. Soc.* **2004**, *126*, 14796–14803.
- (78) Ivanov, V. A.; Bachelier, J.; Audry, F.; Lavalley, J. C. Study of the Meerwein–Ponndorf–Verley Reaction between Ethanol and Acetone on Various Metal Oxides. *J. Mol. Catal.* **1994**, *91*, 45–59.
- (79) Boronat, M.; Corma, A.; Renz, M. Mechanism of the Meerwein–Ponndorf–Verley–Oppenauer (MPVO) Redox Equilibrium on Sn- and Zr-Beta Zeolite Catalysts. *J. Phys. Chem. B* **2006**, *110*, 21168–21174.
- (80) Lewis, J. D.; Van De Vyver, S.; Crisci, A. J.; Gunther, W. R.; Michaelis, V. K.; Griffin, R. G.; Román-Leshkov, Y. A Continuous Flow Strategy for the Coupled Transfer Hydrogenation and Etherification of 5-(Hydroxymethyl)Furfural Using Lewis Acid Zeolites. *ChemSusChem* **2014**, *7*, 2255–2265.
- (81) Foley, B. L.; Bhan, A. Degree of Rate Control and De Donder Relations – an Interpretation Based on Transition State Theory. *J. Catal.* **2020**, *384*, 231–251.
- (82) Harris, J. W.; Arvay, J.; Mitchell, G.; Delgass, W. N.; Ribeiro, F. H. Propylene Oxide Inhibits Propylene Epoxidation over Au/Ts-1. *J. Catal.* **2018**, *365*, 105–114.
- (83) Coblenz Society, I. In *Nist Chemistry Webbook, Nist Standard Reference Database Number 69*; Linstrom, P. J., Mallard, W. G., Eds.; National Institute of Standards and Technology: Gaithersburg, MD (accessed May 11, 2020).
- (84) Herndon, W. C.; Vincenti, S. P. Hydrogen Bonding in Optically Active and Racemic 2-Butanol. *J. Am. Chem. Soc.* **1983**, *105*, 6174–6175.
- (85) Stuart, A. V.; Sutherland, G. B. B. M. Effect of Hydrogen Bonding on the Deformation Frequencies of the Hydroxyl Group in Alcohols. *J. Chem. Phys.* **1956**, *24*, 559–570.
- (86) Knoezinger, H.; Stuebner, B. Adsorption of Alcohols on Alumina. I. Gravimetric and Infrared Spectroscopic Investigation. *J. Phys. Chem.* **1978**, *82*, 1526–1532.
- (87) Errera, J.; Gaspart, R.; Sack, H. Infra-Red O–H Band and Association. *J. Chem. Phys.* **1940**, *8*, 63–71.
- (88) Errera, J.; Mollet, P. Intermolecular Forces and O–H Absorption Bands in Alcohols at 3 $\mu$ . *Nature* **1936**, *138*, 882–882.

- (89) Liddel, U.; Becker, E. D. Infra-Red Spectroscopic Studies of Hydrogen Bonding in Methanol, Ethanol, and T-Butanol. *Spectrochim. Acta* **1957**, *10*, 70–84.
- (90) Langoor, M. H.; Van Der Maas, J. H. On the Competitive Intramolecular H-Bonding in Alcohols with Two Accepting Sites. *J. Mol. Struct.* **1997**, *403*, 213–229.
- (91) Farzaneh, A.; Dejacco, R. F.; Ohlin, L.; Holmgren, A.; Siepman, J. I.; Grahn, M. Comparative Study of the Effect of Defects on Selective Adsorption of Butanol from Butanol/Water Binary Vapor Mixtures in Silicalite-1 Films. *Langmuir* **2017**, *33*, 8420–8427.
- (92) Bregante, D. T.; Potts, D. S.; Kwon, O.; Ayla, E. Z.; Tan, J. Z.; Flaherty, D. W. Effects of Hydrofluoric Acid Concentration on the Density of Silanol Groups and Water Adsorption in Hydrothermally Synthesized Transition-Metal-Substituted Silicalite-1. *Chem. Mater.* **2020**, *32*, 7425–7437.
- (93) Eckstein, S.; Hintermeier, P. H.; Zhao, R.; Baráth, E.; Shi, H.; Liu, Y.; Lercher, J. A. Influence of Hydronium Ions in Zeolites on Sorption. *Angew. Chem., Int. Ed.* **2019**, *58*, 3450–3455.
- (94) Onsager, L. Electric Moments of Molecules in Liquids. *J. Am. Chem. Soc.* **1936**, *58*, 1486–1493.
- (95) Fried, S. D.; Boxer, S. G. Measuring Electric Fields and Noncovalent Interactions Using the Vibrational Stark Effect. *Acc. Chem. Res.* **2015**, *48*, 998–1006.
- (96) Fried, S. D.; Bagchi, S.; Boxer, S. G. Measuring Electrostatic Fields in Both Hydrogen-Bonding and Non-Hydrogen-Bonding Environments Using Carbonyl Vibrational Probes. *J. Am. Chem. Soc.* **2013**, *135*, 11181–11192.
- (97) Boxer, S. G. Stark Realities. *J. Phys. Chem. B* **2009**, *113*, 2972–2983.
- (98) Arunan, E.; Desiraju, G. R.; Klein, R. A.; Sadlej, J.; Scheiner, S.; Alkorta, I.; Clary, D. C.; Crabtree, R. H.; Dannenberg, J. J.; Hobza, P.; Kjaergaard, H. G.; Legon, A. C.; Mennucci, B.; Nesbitt, D. J. Definition of the Hydrogen Bond (IUPAC Recommendations 2011). *Pure Appl. Chem.* **2011**, *83*, 1637–1641.
- (99) Chakraborty, S.; Kumar, H.; Dasgupta, C.; Maiti, P. K. Confined Water: Structure, Dynamics, and Thermodynamics. *Acc. Chem. Res.* **2017**, *50*, 2139–2146.
- (100) Hummer, G.; Rasaiah, J. C.; Noworyta, J. P. Water Conduction through the Hydrophobic Channel of a Carbon Nanotube. *Nature* **2001**, *414*, 188–190.
- (101) Köfinger, J.; Hummer, G.; Dellago, C. Macroscopically Ordered Water in Nanopores. *Proc. Natl. Acad. Sci. U. S. A.* **2008**, *105*, 13218.
- (102) Demontis, P.; Gulin-González, J.; Masia, M.; Suffritti, G. B. The Behaviour of Water Confined in Zeolites: Molecular Dynamics Simulations Versus Experiment. *J. Phys.: Condens. Matter* **2010**, *22*, 284106.
- (103) Rieth, A. J.; Hunter, K. M.; Dincă, M.; Paesani, F. Hydrogen Bonding Structure of Confined Water Templated by a Metal-Organic Framework with Open Metal Sites. *Nat. Commun.* **2019**, *10*, 4771.
- (104) Young, T.; Abel, R.; Kim, B.; Berne, B. J.; Friesner, R. A. Motifs for Molecular Recognition Exploiting Hydrophobic Enclosure in Protein–Ligand Binding. *Proc. Natl. Acad. Sci. U. S. A.* **2007**, *104*, 808.
- (105) Yadav, A.; Jackson, R. M.; Holbrook, J. J.; Warshel, A. Role of Solvent Reorganization Energies in the Catalytic Activity of Enzymes. *J. Am. Chem. Soc.* **1991**, *113*, 4800–4805.
- (106) Krug, R. R.; Hunter, W. G.; Grieger, R. A. Statistical Interpretation of Enthalpy–Entropy Compensation. *Nature* **1976**, *261*, 566–567.
- (107) Krug, R. R.; Hunter, W. G.; Grieger, R. A. Enthalpy–Entropy Compensation. 2. Separation of the Chemical from the Statistical Effect. *J. Phys. Chem.* **1976**, *80*, 2341–2351.
- (108) Krug, R. R.; Hunter, W. G.; Grieger, R. A. Enthalpy–Entropy Compensation. 1. Some Fundamental Statistical Problems Associated with the Analysis of Van't Hoff and Arrhenius Data. *J. Phys. Chem.* **1976**, *80*, 2335–2341.
- (109) Alexopoulos, K.; Lee, M.-S.; Liu, Y.; Zhi, Y.; Liu, Y.; Reyniers, M.-F.; Marin, G. B.; Glezakou, V.-A.; Rousseau, R.; Lercher, J. A. Anharmonicity and Confinement in Zeolites: Structure, Spectroscopy, and Adsorption Free Energy of Ethanol in H-ZSM-5. *J. Phys. Chem. C* **2016**, *120*, 7172–7182.
- (110) Savitz, S.; Siperstein, F.; Gorte, R. J.; Myers, A. L. Calorimetric Study of Adsorption of Alkanes in High-Silica Zeolites. *J. Phys. Chem. B* **1998**, *102*, 6865–6872.
- (111) Eder, F.; Lercher, J. A. On the Role of the Pore Size and Tortuosity for Sorption of Alkanes in Molecular Sieves. *J. Phys. Chem. B* **1997**, *101*, 1273–1278.
- (112) Eder, F.; Stockenhuber, M.; Lercher, J. A. Brønsted Acid Site and Pore Controlled Siting of Alkane Sorption in Acidic Molecular Sieves. *J. Phys. Chem. B* **1997**, *101*, 5414–5419.
- (113) Gounder, R.; Iglesia, E. The Roles of Entropy and Enthalpy in Stabilizing Ion-Pairs at Transition States in Zeolite Acid Catalysis. *Acc. Chem. Res.* **2012**, *45*, 229–238.
- (114) Lazaridis, T. Inhomogeneous Fluid Approach to Solvation Thermodynamics. 2. Applications to Simple Fluids. *J. Phys. Chem. B* **1998**, *102*, 3542–3550.
- (115) Lazaridis, T. Inhomogeneous Fluid Approach to Solvation Thermodynamics. 1. Theory. *J. Phys. Chem. B* **1998**, *102*, 3531–3541.